UNIVERSITY
OF TWENTE.

FACULTY OF MECHANICAL ENGINEERING
CHAIR: PRODUCTION TECHNOLOGY

MASTER THESIS

Evaluating Impact Fatigue Performance of Composite Hulls in High-Speed Crafts

---

DAMEN

IN COLLABORATION WITH DAMEN SHIPYARDS
R&D STRUCTURAL GROUP

Author:
Auke Jaspars
s2141655

Date:
February 2025

Acknowledgement

This research could not have been conducted without the help of several people. I would like to take a moment to acknowledge these individuals. To start, I would like to thank Nick Hoksbergen for guiding the research, supporting the resolution of difficult issues, and answering all possible questions. I would also like to thank Damen Shipyards for making this research possible, especially Frederico Garcia Magalhaes for his guidance from Damen and the many brainstorming sessions at the office. During the research, I also regularly used the facilities of the University of Twente, for which I am grateful; without these facilities, this research could not have been conducted. I would like to specifically thank Nick Helthuis, Bert Vos, and Laurent Warnet for their explanations and guidance in using the test setups. For my mental health, I was fortunately able to rely on my parents, friends, and other family members, who helped me through this process. In particular, I would like to thank my friends of "Studentenhuis Fortes" for temporarily housing me for a few months to conduct my experimental tests at UT.

Abstract

The application of composites in the hulls of high-speed crafts is gaining traction, yet concerns remain about their long-term durability against low-velocity ice impacts. This study experimentally constructs the E-N curve, which tracks the number of impacts until penetration for various impact energy levels, for two material lay-ups: a carbon fiber composite and a composite with an additional protective glass fiber layer. Testing was conducted using a drop weight impact tower and a custom-built setup designed for high-frequency, low-energy impacts. The integration of both test setups yielded complementary results. Additionally, residual stiffness and strength were assessed across various energy levels and impact frequencies. The simultaneous occurrence of different failure modes resulted in complex failure mechanics. Based on the findings, two key design recommendations were made for composite vessels subjected to low-energy impacts. First, while a sacrificial layer is beneficial for mitigating high-energy impacts, it offers limited advantage for low-energy impacts. Second, low-energy impacts cause significantly larger damage areas at the same damage fraction compared to high-energy impacts, leading to reduced structural strength. The findings contribute to the safe design of high-speed craft hulls in ice conditions. These insights can guide designers and engineers in enhancing vessel durability and performance, ultimately supporting more sustainable marine operations.

Contents

Nomenclature

Latin Symbols

$\bar{x}$	Sample mean (-)
A	Contact area (m^2)
a	Constant for relation c_d (-)
$A_{basquin}$	Model fitting parameter (-)
AM	Added mass factor with the corresponding translation or rotation (-)
b	Constant for relation c_d (-)
C_0	Mass reduction factor (-)
c_1	Factor accounting for the probability that the design ice pressures occur in a certain region of the hull(-)
c_a	Factor accounting for the probability that the full length of the area will be under pressure at the same time (-)
c_d	Factor accounting for the influence of the size and engine output of the vessel (-)
c_d	Hull region factor (-)
C_E	Ratio of impact energy to specimen thickness (-)
C_{taylor}	Area coefficient parameter (-)
CV	Coefficient of variation (-)
D_{fC}	Compressive fatigue failure (-)
D_{taylor}	Area coefficient parameter (-)
E_a	Absorbed energy (J)
E_c	Modulus of the core (Pa)
E_f	Modulus of the face sheet (Pa)
E_{crush}	Crushing energy (J)
E_{ice}	Youngs modulus of ice (GPa)
$E_{k.eff}$	Effective kinetic energy (J)
E_{pot}	Potential energy (J)
$E_{REG.exp}$	Experimental Young's modulus of REG material (GPa)
E_{REG}	Young's modulus of REG material (GPa)
$E_{SAC.exp}$	Experimental Young's modulus of SAC material (GPa)
E_{SAC}	Young's modulus of SAC material (GPa)

ex	Constant (-)
F	Measured impactor contact force (N)
$F(ze)$	Probability of exceedance (-)
f_a	Geometrical shape function (-)
f_d	Number of events per meter (1/m)
f_x	Function of ex (-)
F_n	Indentation force (N)
g	Gravitational constant (m/s^2)
H	Drop height (m)
h	Thickness of the specimen (m)
h_c	Thickness of the core (m)
h_f	Thickness of the face sheet (m)
h_{eq}	Equivalent ice thickness (m)
k	Constant for a probability of exceedance (-)
l_0	Reference length (m)
l_a	Load length associated with each structural member (m)
l_i	direction cosine with respective direction (-)
M_{vessel}	Mass of the vessel (kg)
m_d	Mass of the impactor (kg)
$m_{basquin}$	Model fitting parameter (-)
M_e	Effective mass (kg)
N	Amount of cycles till failure (-)
n_{sp}	Number of specimens (-)
P	Actual engine output(kW)
p	Ice pressure (Pa)
p_0	Ice pressure at 1 m^2 (Pa)
$P_{\max}$	Maximum force prior to failure (N)
$p_{0.ICE}$	Nominal ice pressure (Pa)
r	Proportion of hits expected to occur on the considered area (-)
r_i	Radius of gyration in respective direction (m)

S	Applied stress (Pa)
S_{n-1}	Sample standard deviation (-)
t	Time (s)
v	Impactor velocity (m/s)
V_{vessel}	Velocity of the vessel (m/s)
v_i	Initial velocity (m/s)
v_n	Nominal velocity (m/s)
v_{hits}	Total expected number of hits (-)
X	Static strength (Pa)
x_0	Load coefficient (-)
x_i	Measured parameter (-)
X_r	Residual strength (Pa)

Greek Symbols

α	Model fitting parameter (-)
α_{taylor}	Area coefficient (-)
β	Model fitting parameter (-)
Δ	Displacement of the vessel (tonnes)
δ	Impactor displacement (m)
δ_i	Initial impactor displacement(m)
η_l	Yaw moment arm (m)
λ_l	Roll moment arm (m)
μ_l	Pitch moment arm (m)
ν_{ice}	Poisson's ratio of ice(-)
ν_{ij}	Poisson's ratio with respective loading and strain directions (-)
ρ_{ice}	Density of ice (kg/m^3)
σ_{app}	Applied peak stress (Pa)
σ_{CAI}	Ultimate compressive residual strength (Pa)
σ_{max}	Maximum stress (Pa)
$\sigma_{f.ice}$	Flexural strength of ice (MPa)
$\sigma_{t.ice}$	Tensile strength of ice (MPa)
σ_{uC}	Ultimate compressive strength (Pa)
ζ_n	Crushing indentation displacement (m)

1 Introduction

In cold climate regions, vessels navigate through different ice conditions, with the variations depending on their location. The interaction between the hull, the watertight body of the vessel, and ice changes significantly due to these variations in ice conditions. The need for a standardized hull construction spans across all years and the classification societies address this by implementing hull criteria to ensure the structural integrity of the vessel hulls. Typically, these requirements influence the sizing of the vessel's machinery, propulsion systems, and hull stiffening in the ice belt area.

In the maritime sector a type of small vessel plays a crucial role in transportation and security, the high-speed craft (HSC). In the construction of the hulls for these HSC composite material can be the newest development. Composite materials are broadly used in other engineering applications, like aviation or automotive industries, due to their lightweight nature and high strength-to-weight ratio. In an internal study of Damen for the development of a composite HSC, the weight reduction was estimated to 60%. This reduction in weight will enhance the fuel efficiency and operational performance of the vessels. However, the structural design of composite HSCs, especially outside military contexts, remains relatively unexplored. In order to solve the challenges related to operation in icy marine environments a better understanding of different ice conditions is required to be an addition to the already established rules by the classification societies. These rules are right now mainly designed for the use of metallic hulls and adapted for composites material. This adaption often do not address the impact of localized damage and cumulative effects of repetitive low energy impacts on the composites structures.

Research plays an important part in the development of a safe design and operation of vessels in ice conditions. New developments in research aim to get a better understanding in the balance of safe navigation and oversized hull and excessive stiffening. In this research the effect of repetitive ice impacts on the long-term strength of composite sandwich panels used in the construction of the hull of HSC will be investigated. This research will combine the experimental results of impact fatigue and models from the literature to seek a better understanding of the fatigue behavior of composites in icy environments. By optimizing the design due to a better understanding of damage mechanics and residual strength and stiffness, this research will ultimately contribute to safer and more efficient maritime operations.

2 Literature review

2.1 Introduction to level and brash ice

Sea ice and icebergs can be quite problematic for a vessel manoeuvring in cold climates. Almost everyone knows about the story of April 15, 1912 when the Titanic sank after crashing an iceberg. A better understanding of the mechanics of ice loading and how sea ice is classified is a necessity for this research. The World Meteorological Organization classifies sea ice into three main types: new and young ice (ice less than 30 cm thick), first-year ice (ice ranging from 30 cm to 2 m thick), and old ice [1]. Additionally, sea ice can be found in numerous configurations, the two most important ones for this research are called level ice and brash ice. Level ice is characterized by a large and continuous sheet of ice or an ice floe with a mostly uniform thickness. When the mean ice thickness exceeds a certain limit, determined by the ice class of the vessels, the use of an icebreaker will be necessary to break the level ice into much smaller chunks, like when drinking a cocktail you can have a big chunk of ice in your glass or smaller chunks as crushed ice. This "crushed ice" is also referred to as brash ice. The differences in mechanical loading and properties between level ice and brash are important for the structural design of vessels operating in these ice conditions [1].

The HSC will operate in level ice of a maximum thickness of 10 cm and in brash ice after an icebreaker has made an ice brash ice channel. According to the Finnish and Swedish ice class rules these conditions are low ice conditions or ICE-E ice class [2]. In this ice class the vessel is primarily manoeuvring in new and young ice, so the mechanical properties of this ice type will be important for this research.

The study by Timco and Weeks [3] offers an overview of the existing knowledge on the engineering properties of sea ice. In this paper the engineering properties that are included are density, tensile strength, Poisson's ratio and the effective modulus. In this article the properties on first-year and old ice are presented and the relation between other ice properties as salinity, porosity and density. A conclusion from the paper is that a significant scatter observed in the mechanical properties of ice due to differences in micro structure [3]. For this research the important material properties of first-year ice are stated in Table 1.

Table 1: Properties of Ice [3]

Property	**Symbol**	**Value**	**Unit**
Density	ρ_{ice}	920	kg/m^3
Young's Modulus	E_{ice}	1	GPa
Poisson's Ratio	ν_{ice}	0.3	-
Tensile Strength	$\sigma_{t.ice}$	$4.278 \cdot v_T^{-0.6455}$	MPa
Flexural Strength	$\sigma_{f.ice}$	$1.76e^{-5.88\sqrt{v_b}}$	MPa

The tensile strength and flexural strength are stated as relation and do not have a fixed value. The tensile strength is related to the total porosity, v_T, of the ice and the flexural strength is related to the brine volume fraction, v_b. Both these parameters are important to define the failure envelope of ice, the relation that describes when the ice yields under certain stress states. In the case of a vessel manoeuvring through sea ice, the ice failure will occur in flexure. The flexural strength can thus be used for a good approximation for the vessel manoeuvring in ice.

2.2 Ice loading mechanics

Another important mechanism that needs to be elaborated on is the interaction between an ice floe and the vessel. This interaction between the vessel and ice initiates with the localized crushing of a free ice edge at the contact point of the hull. As the vessel sails forward, the contact area and the crushing force reach a maximum over time. The vessel's forward motion induces deflection of the ice sheet along the hull surface, leading to the initiation of bending stresses within the ice sheet until it fractures into multiple smaller ice floes. This interaction between ice floe and vessel hull is schematically shown in Figure 2.1. These reaction forces of crushing and bending that act on the hull structure may generate localized high pressures. After the ice floe breaks from the ice sheet, the vessel's movement forwards forces them to slide along the edge until it aligns parallel to the hull. Eventually, the ice floes submerge and glide alongside the hull until contact can no longer be sustained [4].

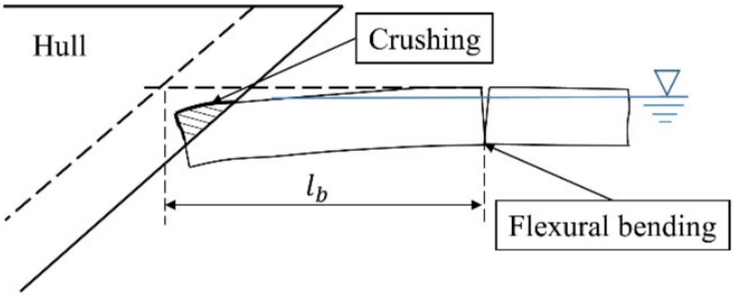

Figure 2.1: Schematic overview ice breaking interaction between a vessel bow and level ice

2.2.1 Ice loading mechanics Daley

To study the forces and the stresses from the ice plate acting on the hull, the energy method is mostly used in literature. This method was proposed by Daley [5] and it offers an efficient method for determining the crushing force and displacement for the ice-hull interaction. The collision of the vessel and the ice sheet is assumed to have one object in motion while the other object stands still. The effective kinetic energy, $E_{k.eff}$, from the vessel corresponds to the energy used for the other object as crushing energy. An assumption made in this relation is that the ice plate has an infinitely large mass, as in this way the effective kinetic energy can be regarded as the same as the total kinetic energy [6]. While this assumption is not entirely accurate, it is effective because, in impact events, the initial material response determines the stresses and pressures, and the bulk of the material does not have sufficient time to respond. The crushing energy can be regarded as the indentation force F_n and the crushing indentation ζ_n, which is the displacement through the ice sheet from the contact point. This crushing energy is found by integrating the force over the indentation.

$$E_{crush} = \int_0^{\zeta_n} F_n(\zeta_n) d\zeta_n \tag{1}$$

To get a derivation for the normal impact force, the kinetic energy will be set equal to the crushing energy equation. The kinetic energy is related to the nominal velocity v_n and the effective mass M_e. Here, the effective mass represents the portion of the vessel's mass that actually contributes to the impact with the ice floe, rather than the full mass of the vessel. A derivation for the effective mass and nominal velocity will be presented later in subsubsection 2.2.2.

$$\frac{1}{2} M_e v_n^2 = \int_0^{\zeta_n} F_n(\zeta_n) d\zeta_n \tag{2}$$

The full derivation for the normal impact force can be found in the paper of Daley [5]. In this paper eight different geometry cases are presented and the derivation of the general equation for all contact cases will be elaborated on this section. The derivation starts with the relation for the normal impact force relative to a geometric parameter, f_a, based on the geometrical shape of the contact case and their function of ex, f_x, based on a constant ex. In literature this constant ex is often taken as $ex = -0.1$. At last this equation is also related to the nominal pressure and the indentation. This creates the following relation:

$$F_n = p_0 \, f_a \, \zeta_n^{fx-1} \tag{3}$$

Where p_0 is the pressure, f_a is geometrical shape function, f_x is the function of ex, and ζ_n is the crushing indentation. The relation for the indentation was derived by combining Equation 3 and Equation 2 and then isolating the indentation. This derivation led to the following relation of the indentation.

$$\zeta_n = \left(\frac{E_{k.eff} \, f_x}{f_a \, p_0}\right)^{\frac{1}{fx}} \tag{4}$$

Implementing Equation 4 into Equation 3 gets

$$F_n = p_0 \, f_a \left(\frac{E_{k.eff} \, f_x}{f_a \, p_0}\right)^{\frac{fx-1}{fx}} \tag{5}$$

With this relation of the normal impact force the load on the vessel hull for different type of contact cases can be predicted.The research of Daley [5] looked at 8 important possible contact cases. The cases relevant for this research are case 1 symmetric V wedge, case 3 right angle edge and case 4 general wedge(normal to hull). The relations for the geometric equation and the formula of ex for their respective contact cases are shown in Table 2 and a schematic overview of the contact case is shown in Figure 2.2. The following steps will be determining the governing contact case related to this research.

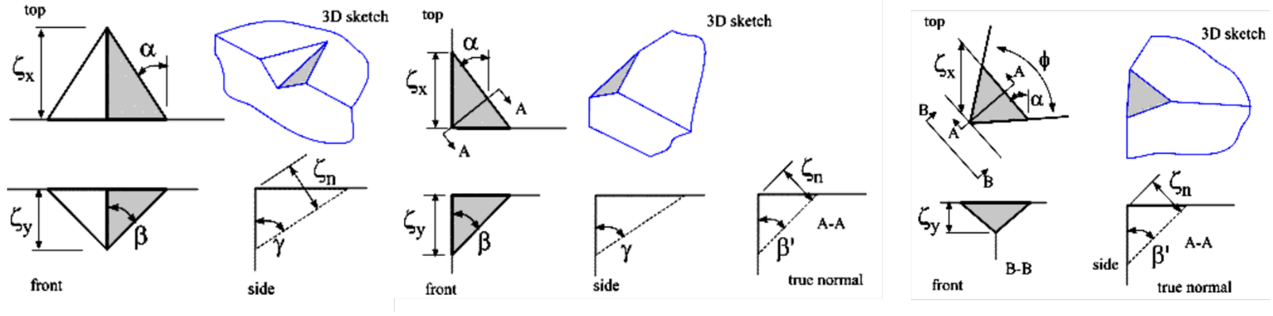

Figure 2.2: Schematic overview contact cases, from left to right contact case 1, 3 and 4 [5]

Table 2: Indentation functions for various contact cases

Case	**Contact Case**	f_x	f_a
1	Symmetric V	$3+2ex$	$\left(\frac{\tan(\alpha)}{\cos^2(\gamma)\sin(\gamma)}\right)^{1+ex}$
3	Right-Angle Edge	$3+2ex$	$\left(\frac{1}{\sin(\alpha)\cos(\alpha)\sin(\beta')\cos^2(\beta')}\right)^{1+ex}$
4	General Wedge	$3+2ex$	$\left(\frac{\tan(\phi/2)}{\sin(\beta')\cos^2(\beta')}\right)^{1+ex}$

2.2.2 Derivation effective mass and nominal velocity

In most cases the effective kinetic energy is equal to the total kinetic energy of the vessel. However in some cases this effective kinetic energy is reduced with the use of a effective mass and a nominal velocity. These cases are also called oblique ice impacts, as shown in Figure 2.3. In the study of Daley [6] the derivation of the nominal velocity and effective mass is derived and this derivation is shown in this section.

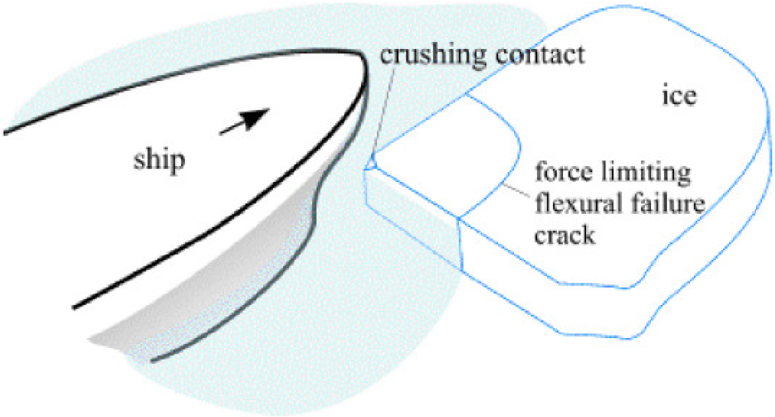

Figure 2.3: Schematic overview oblique impact ice floe [6]

The nominal velocity is determined using the direction cosine times the velocity of the vessel. The x direction is the only cosine involved as the other cosines are equal to zero.

$$V_n = V_{vessel} \cdot l_x \tag{6}$$

where V_n is the nominal velocity, V_{vessel} is the velocity of the vessel and l_x is the x-direction cosine. For the effective mass the mass of the vessel is reduced by a mass reduction factor that is based on the research of Popov [7]. This mass reduction factor accounts for the fact that not the full mass of the vessel contributes to the impact with the ice floe. Instead, only a portion of the vessel's mass effectively interacts with the ice floe. During the impact event, the forces on the hull are not uniformly distributed, but they are concentrated at the contact point causing local deformation. Also the dynamic response of the impact ensures that only mass close to the impact point has sufficient time to respond. This means that the the overall mass involved in the collision needs to be reduced [8].

$$M_e = \frac{M_{vessel}}{C_0} \tag{7}$$

$$C_o = \frac{l_x^2}{1 + AM_x} + \frac{l_y^2}{1 + AM_y} + \frac{l_z^2}{1 + AM_z} + \frac{\lambda_l^2}{r_x^2(1 + AM_{rol})} + \frac{\mu_l^2}{r_y^2(1 + AM_{pit})} + \frac{\eta_l^2}{r_z^2(1 + AM_{yaw})} \tag{8}$$

where M_e is the effective mass, M_{vessel} is the vessel mass, C_0 is the mass reduction factor, l_x, l_y, l_z are the direction cosines, λ_l, μ_l, η_l are the roll, pitch, yaw moment arms, AM is the added mass factor with the corresponding translation or rotation, r_x, r_y, r_z are the mass radii of gyration.

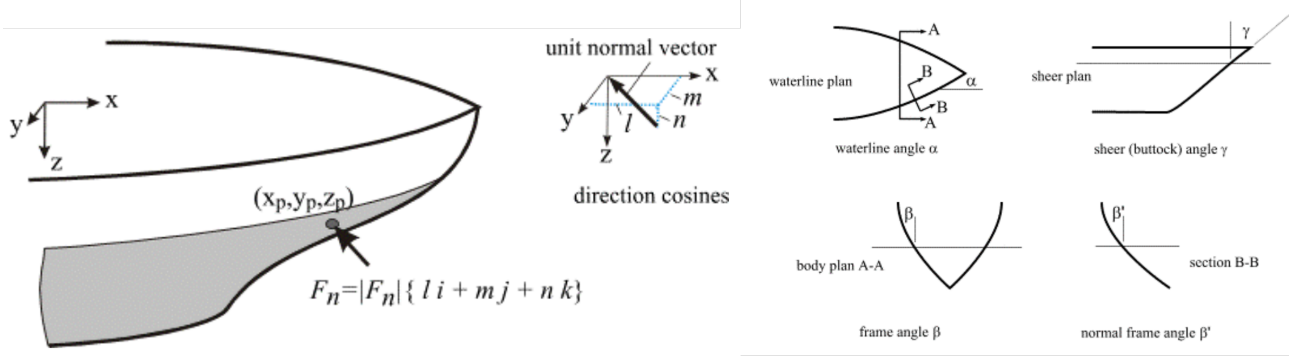

Figure 2.4: Angles and direction cosines overview

The derivation of the direction cosines, the moment arms and the added mass factors are all based on the study of Popov [7]. Their derivation is given as follows

$$tan(\beta) = tan(\alpha)tan(\gamma) \tag{9}$$

$$tan(\beta') = tan(\beta)tan(\alpha) \tag{10}$$

Where α is the waterline angle, β is the force angle, and γ is the shear angle. With these angle derivation the direction cosines can be derived as the following

$$l_x = sin(\alpha)cos(\beta') \tag{11}$$

$$l_y = cos(\alpha)cos(\beta') \tag{12}$$

$$l_z = sin(\beta') \tag{13}$$

The moment arms are

$$\lambda_l = ny_p - mz_p \tag{14}$$

$$\mu_l = lz_p - nx_p \tag{15}$$

$$\eta_l = mx_p - ly_p \tag{16}$$

The added mass terms are as follows

$$AM_x = 0 \tag{17}$$

$$AM_y = 2\frac{T}{B} \tag{18}$$

$$AM_z = \frac{2}{3}\frac{BC_{wp}^2}{T(C_b(l + C_{wp}))} \tag{19}$$

$$AM_{rol} = 0.25 \tag{20}$$

$$AM_{pitch} = \frac{B}{(T(3 - 2C_{wp})(3 - C_{wp}))} \tag{21}$$

$$AM_{sway} = 0.3 + 0.05\frac{L}{B} \tag{22}$$

where T is the draught, B is the breadth, C_{wp} is the water plane coefficient, C_b is the ship block coefficient, and L is the frame span. The squared mass radii of gyration are

$$rx^2 = \frac{C_{wp}B^2}{11.4C_m} + \frac{H^2}{12} \tag{23}$$

$$ry^2 = 0.07C_{wp}L^2 \tag{24}$$

$$rz^2 = \frac{L^2}{16} \tag{25}$$

where C_m is the ship mid-ship coefficient, and H is the height of the load patch.

To conclude with these relations, the effective mass and nominal velocity can now be solved to compute the effective kinetic energy of the impact event of the research case.

2.3 Ice loading estimates models

2.3.1 Design ice load ICE class

In the process of designing a hull for a vessel in ice conditions, engineers use the relations stated in the regulation books of ICE class organization. The most common ICE class organization are Det Norske Veritas (DNV) [9], Bureau Veritas (BV) [10], and the Finish Swedish ice class rules(FSICR) [2]. In this section the relations found in these regulations books are stated and the design pressure for the hull is calculated.

In the three regulation books the relation is an empirical function of the nominal ice pressure times several factors related to vessel dimension, engine output of the vessel and probability that an event happens at a certain location of the vessel. The ICE class that would be used for the vessel of interest in this thesis is the ice load as per class notation ice of ICE-E in DNV, young ice 2 for BV and ICE-IC for FSICR, as the ice conditions in which the vessel is maneuvering are considered low [9][10][2].

$$p = c_d \cdot c_1 \cdot c_a \cdot p_{0.ICE} \tag{26}$$

where c_d is a factor that takes account of the influence of the size and engine output of the vessel, c_1 is a factor that takes into account the probability that the design ice pressure occurs in a certain region of the hull(BV calls this factor c_p) , c_a is a factor that takes into account the probability that the full length of the area will be under pressure at the same time, and $p_{0.ICE}$ is the nominal ice pressure taken as 5.6 MPa. However, in the regulation books of BV the rules state that for YOUNG ICE 2 class that the nominal ice pressure should be taken as 3.0 MPa. The drop in nominal ice pressure can be explained as follows: young ice classes reflect the physical properties of young ice, which are less dense and mechanically weaker compared to older ice types. c_d or the hull region factor is calculated with the following relations [10].

$$c_d = \frac{a\,k + b}{1000} \tag{27}$$

$$k = \frac{\sqrt{\Delta \cdot P}}{1000} \tag{28}$$

Where Δ is the displacement of the vessel (10 ton according to requirements), P is the actual engine output in reality this is 1800 kW. However the regulations state that the engine output can be maximal 750 kW in DNV, 1000 kW in FSICR and BV. Where a and b are given with Table 3 and these are the same for all 3 regulation books. The values of a and b are respectively 30 and 230, as the forward region is more governing and thus results in a higher ice pressure.

Table 3: Hull region factor parameter values [9, 10, 2]

	Forward		**Midship & Aft**	
Parameter	$k < 12$	$k > 12$	$k < 12$	$k > 12$
a	30	6	8	2
b	230	518	214	286

c_a is calculated with the following relations

$$DNV\ and\ BV:\ c_a = \sqrt{\frac{l_0}{l_a}} \tag{29}$$

$$FSCIR: c_a = \frac{47 - 5 * l_a}{44} \tag{30}$$

Where l_0 is the reference length equal to 0.6 m and l_a is the load length associated with each structural member l_a should be taken with Table 4, for every regulation book this table is the same. The structural members at the governing location are transverse frames and their frame spacing is 1 m.

Table 4: Factor l_a calculation values [9, 10, 2]

Structure	**Type of Framing**	l_a
Shell	Transverse	Frame spacing
	Longitudinal	2 x Frame spacing
Frames	Transverse	Frame spacing
	Longitudinal	Span of frame
Ice Stinger	-	Span of stinger
Web Frame	-	2 x Web frame spacing

The value for c_1 is different for every regulation book. DNV state that the factor c_1 should be taken equal to 0.3, BV has a table shown in Table 5 and the value of c_1 should be taken as 0.3, in the FSCIR the value of c_1 should be taken equal to 1 as the hull region is the bow region [9][10][2].

Table 5: Factor values per ICE-class for c_1 [10]

Hull Region	**IA Super**	**IA**	**IB**	**IC**	**ID**	**Young Ice 1**	**Young Ice 2**
Bow	1.00	1.00	1.00	1.00	1.00	0.60	0.60
Midbody	1.00	0.85	0.70	0.50	Not applicable		
Stern	0.75	0.65	0.45	0.25	Not applicable		

The calculation parameters and the results for every regulations are shown in Table 6

Table 6: Design pressure calculation parameters and result

Regulation Organization	$p_{0.ICE}$ (MPa)	c_d	c_a	c_1	p (kPa)
DNV	5.6	0.24	0.77	0.3	307
BV	3.0	0.24	0.77	0.3	167
FSICR	5.6	0.24	0.95	1.0	1267

2.3.2 Ice loading estimate model Masterson

In the article by Masterson and Frederking [11] on ice load as a function of contact area, the ice pressure can be described using a simple relation to the contact area. This relation is stated in Equation 31, where the ice pressure, p, is derived from the contact area, A, and a constant k. Two values for the constant, k, are presented in [11]. A value of $k = 8.1$ is provided for a probability of exceedance of 5%, and a value of $k = 13$ is given for a probability of exceedance of 0.1%. This k basically acts like a safety factor, the magnitude of choice is related to the design specifications.

$$p = kA^{-0.5} \tag{31}$$

2.3.3 Ice loading estimate model Taylor

Another model for estimating ice loading was developed by Taylor et al. [12] based on a probabilistic approach. In this model, the ice load is determined by a load coefficient, x_0, the probability of exceedance, $F(z_e)$, the total expected number of hits, v_{hits}, the proportion of hits expected to occur on the considered area, r, and an area coefficient, α_{taylor}. The ice load is calculated according to the formula presented in Equation 33, utilizing the equation for the area coefficient given in Equation 32 with the parameters C_{taylor} and DC_{taylor}.

$$\alpha_{taylor} = C_{taylor} a^{D_{taylor}} \tag{32}$$

$$p = x_0 + \alpha(-ln(-ln(F(z_e))) + ln(v_{hits}) + ln(r)) \tag{33}$$

2.3.4 Ice loading estimate model Rahman

In the research of Rahman et al.[13], they utilized the ice load estimation method proposed by Taylor et al. They gathered data from three distinct ice covers encountered by a lifeboat operating in brash ice conditions. This dataset is presumed to provide a more accurate representation of the ice loads experienced by high-speed crafts. The frequency of impacts is measured as the number of impacts per unit distance, represented as a multiple of the length of the route covered by the high-speed craft.

The model of Taylor [12] can be used to estimate the pressure on the hull of the vessel. The coefficient of the datasets of Rahman [13] and Taylor [12] are used to calculate the ice load estimate pressure. The frequency of impact is calculated with the model of Bridges [14], discussed in subsection 2.5. The coefficient and the results of these calculations are stated in Table 7. From these results it can be seen that the datasets of Taylor [12] have a big scatter and the values are higher than the design pressure advised by the ICE pressure formulation. The results of Rahman [13] are much closer to each other and the values have a similar magnitude as the ICE design pressure. Both studies collected in-situ data on ice loading to estimate their parameters for the model. To compare the design pressure with the theoretical model, the study of Rahman [13] will be considered since the parameters used in that research are for different ice concentrations. Youngs ice class 2 generally has a low ice concentration, the similarity in the results of the design pressure and the model can be explained in that matter. This also means that the ice design pressure is a suitable relation to estimate the ice loading on the hull.

Table 7: Ice loading estimates from Taylor and Rahman models

Model	**Dataset**	x_0	f_d	r	$F(ze)$	α	p (kPa)
Taylor	Polar sea (Bering ’96)	0.15	83.44	0.14	0.5	0.12	489
	Polar sea (N. Bering ’83)	0.15	83.44	0.14	0.5	0.28	941
	Oden	0.15	83.44	0.14	0.5	1.11	3285
Rahman	High ice concentration	0.029	83.44	0.14	0.5	0.068	221
	Medium ice concentration	-0.002	83.44	0.14	0.5	0.068	190
	Low ice concentration	0.006	83.44	0.14	0.5	0.054	159

The analysis conducted in this study employed several empirical models to estimate ice loads on the hull of the vessel. These models have been compared with design pressures calculated in subsubsection 2.3.1 proposed by ICE class organizations (DNV, BV, and FSICR) to assess their applicability for vessels operating in low ice concentration environments.

The Taylor model [12] results exhibit a high degree of scatter, with pressure estimates significantly exceeding the design pressures recommended by the classification institutions. This overestimation suggests that the Taylor dataset, particularly the Oden data, may not be appropriate for vessels operating in low ice concentrations.

The Rahman model [13] produces more consistent pressure estimates, with values that are both closely grouped and comparable to the empirical design pressures. Specifically, the Rahman low ice concentration dataset yields a design pressure of 159 kPa, which is closest to the BV recommended pressure of 167 kPa. This alignment suggests that the Rahman low ice concentration dataset provides a reliable basis for estimating ice loads for vessels operating in similar conditions.

2.4 Impact mechanics

Impact is the process of one object coming forcibly into contact with another object, for example a hammer hitting a nail or in this case a vessel hitting an ice shoe. In the period of contact the pressure in this contact area results in local deformations and indentation. The contact pressure has a resultant force of action/reaction that would act in the opposite direction of the two colliding objects. At the start of the contact this resultant force is increasing as the indentation increases, this results in a decreasing of the relative velocity between the two objects and at a certain point this velocity decreases to zero. After this point the energy stored during this compression is used to drive the two bodies apart until they separate of each other [15].

2.4.1 Impact configuration and classes

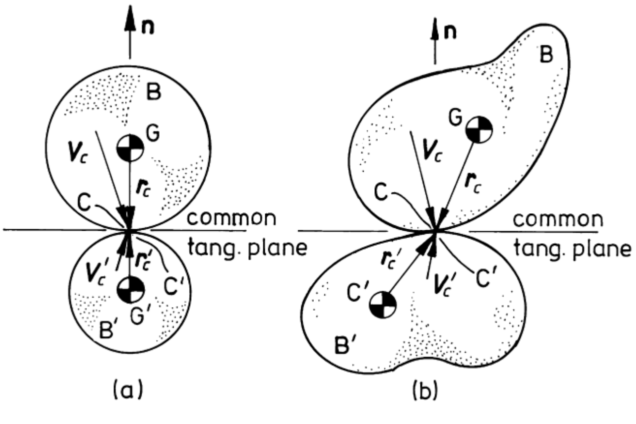

Figure 2.5: Schematic overview central impact and eccentric impact[15]

Two configurations exist for impacts of two bodies, a central impact configuration and an eccentric configuration. Both types of configuration are shown in Figure 2.5. With a central impact the centers of gravity of both bodies are in the normal line and thus their position vectors are parallel to the normal line. For a vessel ice floe impact this could be seen as the vessel hitting the ice floe straight, assuming the center of gravity lies on the direction line of the vessel. For an eccentric impact at least one of the bodies' center of gravity is not on the normal line and their position vectors are not parallel to the normal line. This can be seen as an oblique or shoulder impact of the vessel to the ice floe [15].

Literature there are 4 classes of impact: particle impact, rigid body impacts, transverse impact on flexible bodies and axial impacts. For this case only the transverse impact is important. This type of impact occurs when at least one of the bodies, such as the ice, undergoes bending due to the pressure at the contact area. The location of this bending is not at the contact area but at a significant distance from the contact area. This bending decreases the pressure at the contact area and extends the contact duration. The collision between a vessel and an ice floe is similar as explained in subsection 2.2[15].

The analysis of transverse impacts on structural components is highly dependent on the flexural rigidity of the structures [15]. In a more general impact case the deformations are assumed to be local as the surrounding material remains rigid. However, transverse impacts induce this significant bending deformation that influences the body. The response of the structure is primarily dominated by these flexural deformations during the contact period, making the bending stiffness a key factor in the contact stiffness determination.[15][16]

2.5 Statistical models for predictions frequency of impacts

The model of the research by Bridges [14] is not verified for small ice thickness values and may not be useful for this research. However, the model will still be explained as an estimation for the number of impacts is an important parameter for this research. In the research of Bridges et al. [17], the amplitude frequency is theoretically governed by the size of floes (d_{floe}) undergoing bending. This floe size is contingent on speed, with higher speeds resulting in smaller floe sizes, as elucidated by Varsta [18]. Conversely, the speed of the vessel is affected by the thickness of the ice. Consequently, Bridges [14] proposed the subsequent formulation for the frequency of impact per meter sailed. This relation is dependent on the equivalent ice thickness and a hull region factor. This factor takes into account the size and engine output of the vessel and also the region on the vessel[19].

$$f_d = c_d \frac{1}{10.4 h_{eq}^{3/4} - 2.0 h_{eq} + 1.18} \tag{34}$$

Where f_d is the number of events per meter, h_{eq} is the equivalent ice thickness in meters, c_d is the hull region factor.

Furthermore, Bridges [17] plotted the theoretical relation for frequency of impact and the available ice impact data as illustrated in Figure 2.6. As you can see there is a notable difference in the theoretical model and the available data and there is also a significant scatter within the data. Bridges [14] explained that this was a result of different ice conditions encountered by the vessels. The difference in the theoretical model and the data can be explained by the probability that the sensor did not register an ice floe, as this could already have been broken by a different part of the vessel hull. There is also the issue that limited data exist for small ice thickness values of below 0.4 m [17].

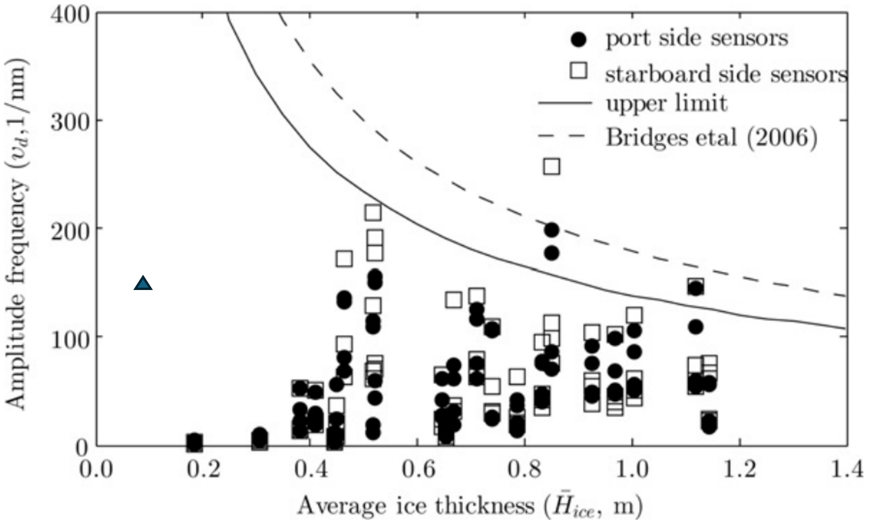

Figure 2.6: The impact frequency per distance compared with available data and also with the impact frequency for the vessel of interest(blue triangle) [20]

An estimate of the frequency of impacts has been calculated and the calculation parameters and the result are shown in Table 8. The number of impacts per meter traveled is 0.08 and thus the amount of events per nautical mile will be 148. If you look at the Figure 2.6 this result does not follow the trend line made by the model of Bridges [14], as the vessel for this research has a different hull region factor. However the magnitude of the result is within the range of the magnitudes of the measured data.

Table 8: Calculation parameter frequency of impacts

Model	h_{eq} (m)	a	b	k	c_d	f_d (1/m)
Bridges	0.1	30	230	0.20	0.24	0.08

2.6 Composites for marine application

"The definition of a composite material according to literature is as follows: 'A composite material is a combination of two materials with different physical and chemical properties.' There can be quite a few combinations of materials made in this world, so in this research the combination of fibres and polymers or fibre reinforced polymers(FRP) will be considered.

FRP consist of two main components: fibres and a resin or matrix material. The primary role of the fibres is to provide strength and stiffness to the material. Their arrangement within the composite enhances mechanical properties, particularly when aligned with the loads. However, perpendicular to the direction of the fibres, there is not a significant increase in stiffness, as the fibres tend to act more as stress concentrators in that direction. In most FRP, different fibre orientations are utilized, allowing the material to exhibit stiffness and strength in various directions, always being in-plane. The matrix material is typically a polymer that acts as an adhesive for the fibres, effectively encapsulating them within the composite. This configuration improves the composite's ability to withstand compressive loads, as the resin provides support to the fibres [21][22][23].

FRP materials are nowadays broadly used in different fields of engineering, like aerospace, automotive, or construction. The benefit of FRP over steel is that they have a significantly lower density with relatively good stiffness and strength, as can be seen in Table 9. This table is a result of the study into the mechanical properties of different FRP material types and steel [24]. The marine industry is also using FRP in the construction of vessels [25]. This research will look at composite hulls of a high-speed safety vessel. The broad range in mechanical properties for FRP materials can be attributed to several factors, including the type of fibres used, the fibre volume fraction, and the type of polymer matrix. These factors contribute to the variability in mechanical properties, making FRP a versatile material for various applications.

Table 9: Mechanical properties of FRP types and steel [24]

Property	**CFRP**	**GFRP**	**AFRP**	**BFRP**	**Steel**
Density (g/cm^3)	1.50–2.10	1.25–2.50	1.25–1.45	1.90–2.10	7.85
Tensile Strength (MPa)	600–3920	483–4580	1720–3620	600–1500	483–690
Young's Modulus (GPa)	37–784	35–86	41–175	50–65	200
Elongation (%)	0.5–1.8	1.2–5.0	1.4–4.4	1.2–2.6	6.0–12.0
Coefficient of Linear Expansion ($10^{-6}/°C$)	-9.0–0.0	6.0–10.0	-6.0–2.0	9.0–12.0	11.7

2.6.1 Sandwich composite structures

For hull structures in the marine industry, sandwich composites materials are used. These sandwich structures are also used in other engineering applications. A sandwich structure consists of two skin sheets (the bread of the sandwich) and in the middle a core material(the filling of the sandwich). The skin sheets are made out of FRP using carbon or glass fibres with an epoxy matrix. The purpose of the skin sheets is provide the stiffness and the strength of the material in the plane of the laminate and also absorb the contact load acting on the laminate. These skin sheets are significantly stiffer and stronger compared to the core material, which is mostly a non-rigid and light material. The main purpose of this core material is to provide a distance between the two skin sheets. This is ideal, as the bending shear stresses will dissipate, providing high bending stiffness, since the materials are primarily loaded in tension or compression. An additional feature of this core structure is that it will provide a good thermal isolation. This core structure consists mostly out of a honeycomb structure or a foam structure. In the marine industry commercially a core structure of pvc foam is used [25][26].

For this research, two different sandwich structures will be considered:

1. **Quasi-Isotropic Carbon Fibre Epoxy with Woven E-Glass Layer (REG)**: This structure consists of quasi-isotropic carbon fibre epoxy face sheets with a high-density PVC foam core. Additionally, it includes a small layer of woven E-glass oriented at 0/90 degrees (REG).
2. **REG with Sacrificial Quasi-Isotropic E-Glass Fibre Epoxy Layer (SAC)**: This structure features the REG with a sacrificial layer consisting of quasi-isotropic E-glass fibre epoxy on one side.

2.6.2 Failure modes and mechanics sandwich structures by impact load

FRP composites loaded by an impact experience a load with a short time span perpendicular to the plate. This results in compressive stresses in the top layer and tensile stresses in the bottom layer, will primarily experience shear stresses, with some compression and tensile stresses. These stresses can lead to different failure modes in each of these components and additionally, the bond between these components could fail through delamination due to the steep transition in stress across the interface.

A schematic overview of the possible failure modes is shown in Figure 2.7 and these failure modes will be elaborated on [27][28].

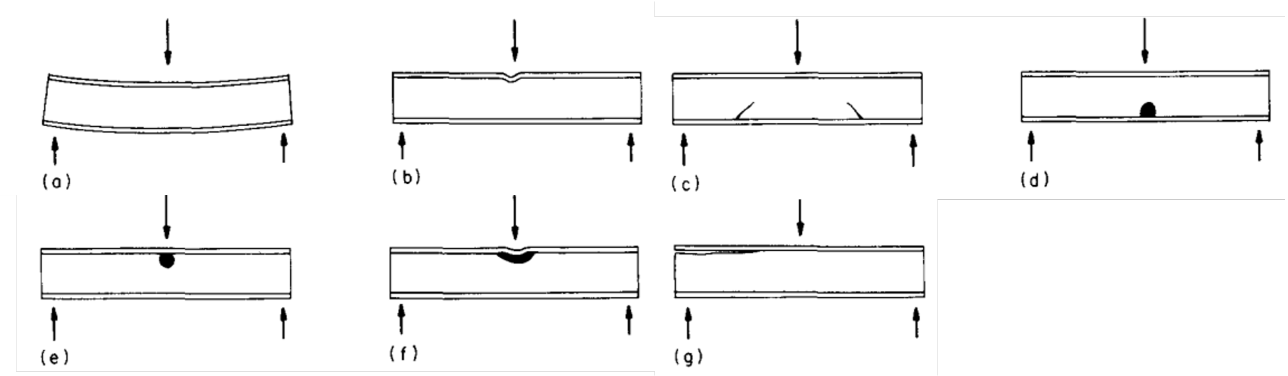

Figure 2.7: Schematic overview failure modes: face yielding (a), face wrinkling (b), core shear (c), core tensile yield (d), core compressive yield(e), core identation (f) and debonding (g) [27]

The failure modes that are shown in the face sheet are face yielding and face wrinkling. Face yielding is the fracture of the face sheet. This can happen when the equivalent stress equals the yield stress of the face sheet material. Face wrinkling is a small local buckling by compression of the face sheet. This wrinkling can be seen as a small wave formation on the face sheet. In the study of Heath [29] a relation of the critical wrinkling stress was formulated [30]. This relation is given by

$$\sigma_{cr} = (\frac{2}{3}\frac{h_f}{h_c}\frac{E_c E_f}{(1-\nu_{12}\nu_{21})})^{1/2} \tag{35}$$

where h_f and h_c are the thickness of the face sheet and core, E_c and E_f are the moduli of the face sheet and core, ν_{12} and ν_{21} are the Poisson's ratio with their respective loading and strain directions.

The failure modes that are expected in the foam core are core shear, core tensile yield and core compressive yield. These fractures happen in the core when the stress in their respective load directions are equal to the yield stress of their respective load directions. For the impact load the most common failure mode will be core shear failure as this shear stress will be the most dominant one for a load perpendicular to the material. There are situations in which the material will experience higher normal stresses than the shear stresses. In these cases the tensile and compressive failure of the core will take place. However, the load in these circumstances will be a multi axial state stress and for the impact load this is not expected [28][31].

The failure modes that are expected in the combination of the core and face sheet are indentation and debonding. Indentation is a failure mode characterized by significant localized deformation resulting from a load. This indentation is a result of a high and concentrated load. Impact loads or static indentation are the main cause of this failure mode to occur [28]. Debonding is the failure in which the core and the face sheet are separated. This failure occurs when the adhesive bond between both elements breaks due to the load applied. This often occurs when cracks exists within the adhesive, so the residual strength of the adhesive is already lowered and stress concentrations can arise around these cracks or defects. These cracks can be created during the manufacturing process due to an improper application of the adhesive in which voids or weak spots are created. These voids and weak spots act as stress concentrators, initiating cracks [32].

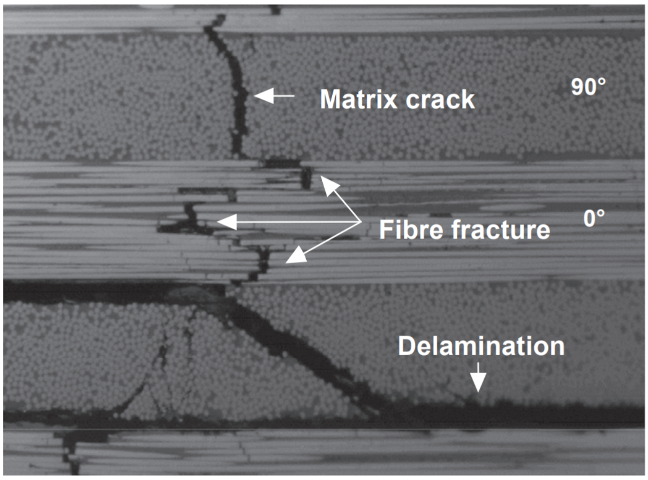

Figure 2.8: Overview of matrix cracking, fibre failure and delamination examples optical microscopy

To further visualize these failure modes, optical microscopy examples are shown in Figure 2.8. The figure highlights three key damage mechanisms: matrix cracking, fibre fracture, and delamination. Matrix cracking appears as sharp lines within the resin, indicating broken paths in the matrix, which can propagate and weaken the structural integrity of the composite. fibre fracture occurs when the stress exceeds the fibre's strength, causing the fibres to break, often resulting in a jagged fracture surface. Delamination is evident as voids or separations between composite layers due to interfacial failures.

Lim [33] made a failure mode map for impact loading on glass fibre epoxy composite with a core material of PVC foam (some grades from HT50 till HT110). This failure map is shown in Figure 2.9. In the research of Lim [33], they looked at the failure modes for different material configurations. They looked at the relation of increasing core density and increasing thickness ratio between the face sheet thickness and core thickness. For the sandwich structure used in the vessel of interest the ratio between face sheet thickness and core thickness is 0.05 and the density is 200 kg/m3, both values lie outside the range of parameters considered in study of Lim [33]. However, an assumption can be made that the failure by impact happens in the face sheet.

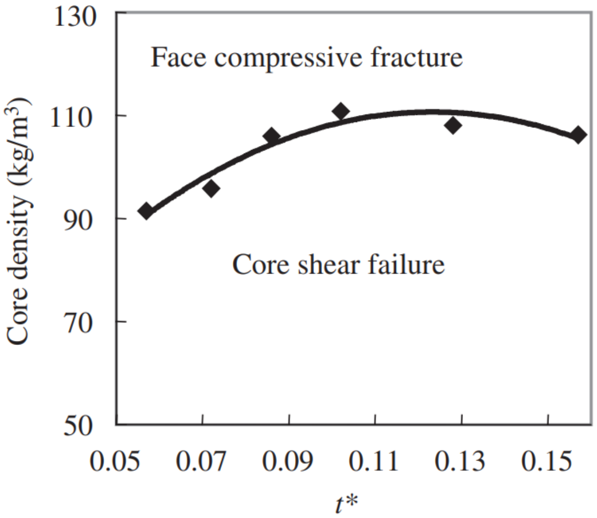

Figure 2.9: Impact failure mode map of sandwich structure of the ratio $t^* = t_f/t_c$ against the core density [33]

2.6.3 Impact fatigue composites

Fatigue is the degradation of the mechanical properties of a material under cyclic loading. This loading is individually not capable of causing the total failure of the material, but the damage from multiple cycles can accumulate, leading to the total failure of the material. Mechanical fatigue and impact fatigue share similarities, as both involve the progressive deterioration of a material due to repeated loading. However, there are key differences:

- **Mechanical Fatigue**: This occurs under cyclic loading where the stress is applied gradually over many cycles. The primary factors influencing mechanical fatigue are the stress amplitude, mean stress, and the number of cycles.
- **Impact Fatigue**: This involves failure due to repetitive low-energy impacts. Each impact may not be sufficient to cause immediate failure, but the cumulative effect of multiple impacts can lead to fatigue failure. Impact fatigue typically involves higher strain rates compared to mechanical fatigue, which can result in different material responses.

While both types of fatigue involve the accumulation of damage over time, the nature of the loading (cyclic vs. impact) and the strain rates involved are significant distinguishing factors. The strain rate experienced in impact fatigue is significantly higher than the strain rate of mechanical fatigue. The strain rate is closely related to the behaviour of the material, especially for polymer and polymer matrix composites, to the load, the energy dissipation of the material and the damage development within the material[34]. A high strain rate limits the time that the material has to react to a certain load before damage develops within the material. A higher strain rate can mean that the material will have a brittle behaviour instead of a more ductile behaviour. This brittle behaviour means that the crack propagation will accelerate and lead to more catastrophic failure, as the mechanism for energy-dissipation has limited time to occur. However, this brittle behavior also results in higher stiffness and strength for the material, primarily due to the applied strain rate. In polymers, stiffness, and strength are notably influenced by the strain rate [34].

The stress-strain curves inFigure 2.10 illustrate how materials behave differently under varying strain rates. The red curve represents a brittle material, which has a higher initial slope, indicating increased stiffness and strength, but also a more abrupt failure, characteristic of brittle behavior. In contrast, the blue curve represents a ductile material, which has a lower initial slope and a more gradual failure, indicating that the material can undergo more deformation before failure.

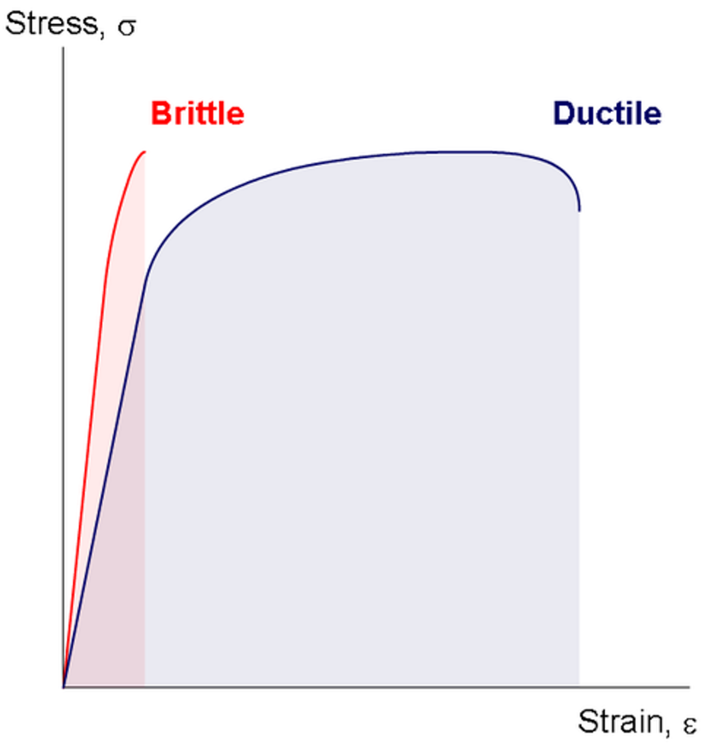

Figure 2.10: Stress-strain curves for brittle and ductile materials

The research conducted into impact fatigue of composites and the failure modes related is limited. The mechanism behind the fatigue of composites under impact loading remains unclear. The importance lies in identifying the potential accumulation of damage that is created by repetitive low energy impacts [34].

2.7 Experimental impact testing

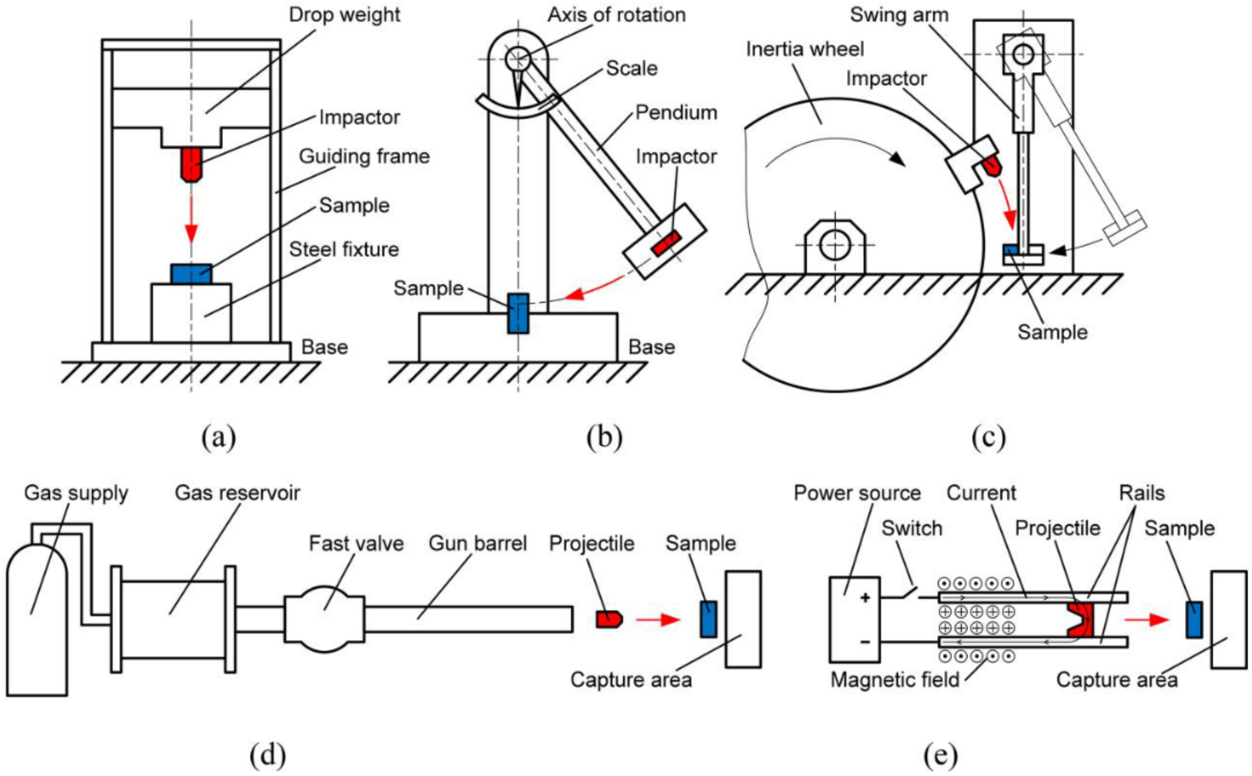

Figure 2.11: Schematic overview of the impact testing methods; (a) drop weight impact test, (b) pendulum impact test, (c) inertia wheel impact test, (d) gas gun impact test and (e) electromagnetic launcher impact test [35]

Experimental impact tests are important in the assesment of the performance of materials under impact conditions. These tests provide insights into material resistance, energy absorption capabilities, and failure modes. In literature the experimental impact tests are divided in classes by the magnitude of the impact velocity. The four classes are low, medium, high and hypervelocity. The classes with their corresponding impact velocity ranges and their typical test methods are listed in Table 10. While each test method has its limitations and potential errors, there is no specific preference for a particular method. Nevertheless, all methods yield similar results, with variations in ease of preparation, execution, and tolerance for errors [36]. A schematic overview of the different test setups is displayed in Figure 2.11.

Table 10: Classification of impact tests

Impact Test	**Velocity (m/s)**	**Test Method**
Low Velocity	<10	Drop weight, pendulum, inertia wheel
Medium Velocity	10–50	Inertia wheel, servo hydraulic, gas gun
High Velocity	50–1000	Gas gun, electromagnetic launcher
Hyper Velocity	2000–5000	Light gas gun, electromagnetic launcher

The drop weight impact test method involves raising an impactor to the desired height and then releasing it, resulting in the impactor colliding with the test specimen. One advantage of this method is that it does not necessitate specific specimens with standard dimensions, unlike other low-velocity test methods [37]. This advantage ensures that more complex geometries and parts can be tested.

Other low-velocity impact test methods include Charpy and Izod, which utilize a pendulum hammer to impact the specimen from a fixed height. The main difference between Charpy and Izod test is in the position of impact on the specimen and the method of specimen clamping. In the Charpy method, the specimen is secured at both ends and impacted in the center, whereas in the Izod method, the specimen is clamped on its lower half and struck on its upper half [38]. These methods are primarily used to assess the impact toughness of specimens and compare them to other composite materials [35].

The first medium-velocity impact test method is the inertia wheel impacting testing method. This approach resembles the pendulum test methods but offers more consistent and increased impact velocities of up to 20 m/s [38]. Another method for achieving medium velocity is the servo-hydraulic method, which shares a design similarity with the drop weight method but utilizes servo-hydraulics to achieve the acceleration instead of the gravitational acceleration [39].

The gas gun impact test employs a method wherein a rigid or flexible projectile is propelled from a barrel towards the test specimen. The necessary pressure to accelerate the projectile is generated using compressed air. An adaptation of the gas gun for achieving higher velocities is known as the light-gas gun, which utilizes compressed helium or hydrogen. These lighter gases have the capability to get greater maximum velocities compared to compressed air [40].

The electromagnetic launcher is capable of achieving the highest velocities. In this test setup, a magnetic field is generated by the flow of current through the rails and the projectile. This magnetic field exerts an electromagnetic force, known as the Lorentz force, which accelerates the projectile and propels it towards the test specimen [41].

In this research impact fatigue for composite sandwich panels will be considered and an energy vs number of cycles to failure diagram will be constructed. The experimental set up that will be used is the drop weight impact test for the low cycles region and for the high cycles region there will be an experimental setup constructed based on a gas gun setup with the use of compressed air and commercial air soft parts, used in the research of Johansen [42]. In subsection 2.9 the E-N curve will elaborated further on and in subsubsection 4.2.1 the single point impact fatigue test (SPIFT) setup will be further explained.

2.8 Compression after impact test

Impact testing is often associated with a compression after impact test(CAI). As the name of the experimentent suggest the post-impact test specimen is subjected to a compressive load until failure. Similar to the case of this research, the impact load of the ice floe on the ship hull will subject the face sheet of the sandwich structure to compressive stresses in the lay up. The result of this test is the residual compressive strength of the specimen. The test specimen is placed in a base assembly supported on both sides and at the bottom. From the top a top assembly applies the load downward. The test procedure is according to ASTM D7137/D7137M – 17 [43].

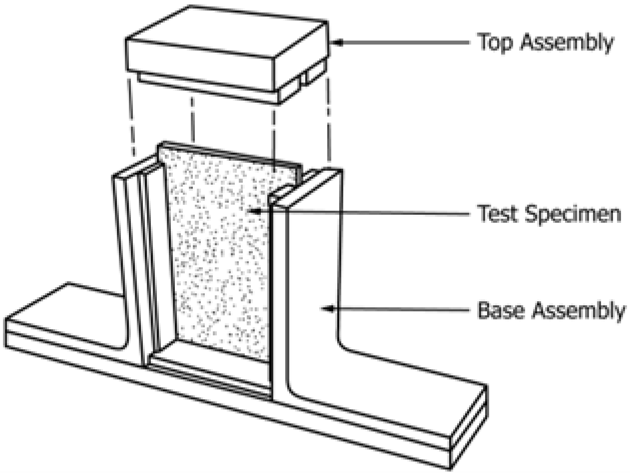

Figure 2.12: Schematic overview CAI setup [43]

From literature, it is stated that the compressive strength after impact is the weakest of the residual properties of the laminate. This is due to the local instability resulting from delamination. Delamination divides the laminate into sub-laminates with significantly lower bending stiffness, as the load is distributed over a smaller area. This reduced bending stiffness makes the laminate more susceptible to buckling under compressive loads. The three common failure modes resulting from this load are global buckling of the laminate, local buckling of a sub-laminate, or a combination of both failure modes [44].

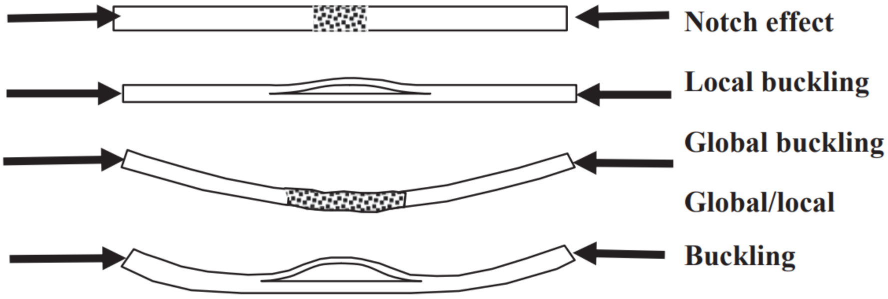

Figure 2.13: Schematic overview failure modes in CAI [45]

In Figure 2.13, a schematic overview of these failure modes is shown. Damage modes such as notching, global and/or local buckling, or combinations of these modes can dominate depending on the extent of the damage introduced by the impact. These failure modes can also interact, leading to complex behavior.

2.9 S-N curve

In subsubsection 2.6.3 the process of fatigue has been discussed. In literature there have been two approaches addressing this fatigue damage. The first approach focuses on the individual cracks utilizing fracture mechanics parameters, such as the stress intensity factor [46]. The other one is to address this fatigue damage with the cracks collectively including crack initiation at a relatively large scale [47]. This collective approach necessitates an S-N curve model, where S is the stress level and N is the number of fatigue loading cycles to failure at this stress level. The S-N curve model is typically represented as a linear function on a log-log or lin-log scale to present the relationship between fatigue life related to fatigue damage [48]. The S-N curve model would be the most beneficial for this research as the repetitive impacts of the ice shoes on the hull need to be modelled collectively.

S-N curve models are used in traditional bulk materials, such as polymers, ceramics, and metals, as well as in composite materials. Composites show different damage types compared to traditional materials. One important aspect is that composites exhibit multiple failure modes, and each failure mode has an associated S-N curve. These failure modes include fibre breakage, matrix cracking, delamination, and fibre-matrix debonding. Despite these differences, a substantial difference in S-N curve measurement between these material types is not noted in literature [48]. An S-N curve is crucial in characterizing fatigue test results from specimens but is also important for the prediction of remaining fatigue life, involving fatigue damage quantification and stress ratio effects [48]. Therefore, the S-N curve will be a useful tool in this research for the prediction of the remaining lifetime, the residual strength, damage quantification and the characterization of the relation between impact energy and cycles till failure.

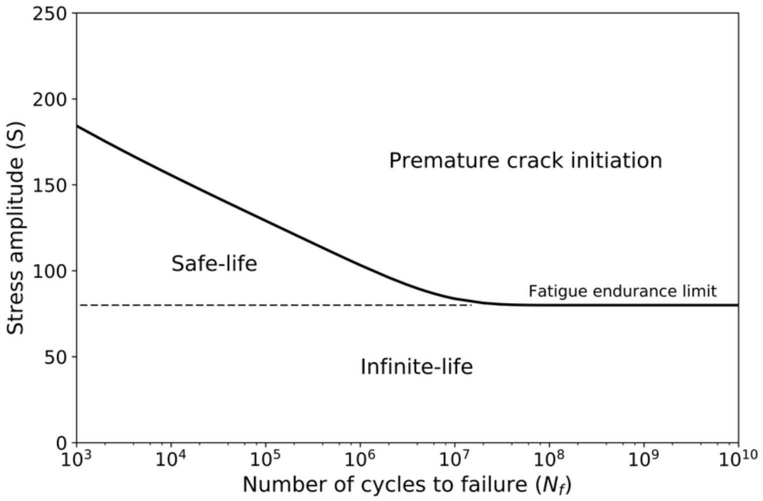

Figure 2.14: Schematic overview S-N curve[49]

In Figure 2.14 a schematic representation of the S-N curve is shown. The curve can be divided in three regions: the infinite life, the safe-life and the premature crack initiation region. The infinite life region is bounded by the plateau value that is also called the fatigue endurance limit. Most of the materials show a plateau value at $N_f = 10^6$, where materials subjected to a stress magnitude of lower than this fatigue endurance limit will show an infinite life. In the safe life region the material is subjected to a stress magnitude of higher than the fatigue endurance limit but the number of cycles is lower than the number of cycles till failure. The premature crack initiation region occurs when for a certain stress magnitude the amount of cycles exceeds the number of cycles till failure [49].

S-N curve models are developed to fit the experimental data from fatigue test specimens subjected to a constant magnitude of stress and loaded at a constant stress ratio. The first model and in practice most used model was developed by Basquin [50]. This model is based on fitting with the use of a power law, shown in Equation 36. While the Basquin model is commonly used and straightforward for parameter determination, it may not always provide a perfect fit to experimental data. Nonetheless, it remains a practical choice due to its simplicity and ease of parameterization.

$$S = A_{basquin} * N^{m_{basquin}} \tag{36}$$

where S is the applied stress, $A_{basquin}$ and $m_{basquin}$ are model fitting parameters and N is the amount of cycles till failure.

2.10 Residual strength and stiffness model

subsubsection 2.6.3 discusses the various types of damage that can occur due to fatigue loading. This damage propagation within the material will eventually lead to material failure, but before that the material will go through a process of stiffness and strength reduction. This damage propagation starts at the weak points of the composite after a few cycles. The regions that are mostly considered as weak points are the region where the concentration resin is high, local fibre-matrix debonding regions or regions with voids in the matrix. This damage propagation results in a decrease of the load-supporting capabilities of the individual ply and which leads to the transfer of the load to adjacent plies. Resulting in more severe types of damage such as delamination and local fibre breakage [51].

2.10.1 Residual stiffness

In progressive fatigue damage modeling, stiffness degradation resulting from matrix cracking is considered at each loading cycle. Research indicates that there is minimal stiffness degradation in the fibre direction. Therefore, in literature, mostly stiffness degradation in the matrix direction is considered [51]. Various models have been proposed for predicting stiffness degradation, among which the nonlinear model proposed by Eliopoulos [52] has been shown to fit experimental data with high accuracy. Thus, the nonlinear regression described by Equation 37 is employed for predicting stiffness degradation.

$$\frac{E_2}{E_2^0} = 1 - (1 - a_2)(\frac{n}{N})^{b_2} \tag{37}$$

2.10.2 Residual strength

In composite layups subjected to cyclic loading, it has been observed that the laminate strength decreases with the number of cycles. In literature there is a general agreement that this strength reduction can be categorized into three stages [51]. In the initial stage, roughly constituting the first 10% of the fatigue life, significant strength degradation occurs due to early fatigue damage mechanisms like matrix cracking. Following this, degradation continues at a slower rate until approximately 90% of the fatigue life. At this juncture, the strength degradation rate suddenly accelerates due to fibre fracture and persists until the residual strength matches the maximum applied stress. At this critical point, the degradation pattern transitions from gradual to sudden degradation rules [51].

Various models have been proposed to predict the trend of residual strength over cycles. Among them, the model suggested by Shokrieh et al. [53] has been reported to provide more accurate predictions

$$(\frac{X_r - \sigma_{max}}{X - \sigma_{max}})^{\alpha} = 1 - (\frac{log(n) - log(0.25)}{log(N) - log(0.25)})^{\beta} \tag{38}$$

Where X_r is the residual strength, X is the static strength, σ_{max} is the maximum stress, α and β are fitting parameters, n is the number of cycles, N is the number of cycles till failure In this research the residual strength model of Shokrieh [53] will be used to determine the residual strength at various fractions of the amount of cycles to failure. This residual strength model will give various important insights for the life prediction model.

3 Research Objectives

3.1 Main research question

In this research, the objective is to get a better understanding of the impact fatigue characteristics to ice loading of sandwich fibre reinforced composites used in marine application. This is achieved by obtaining an S-N curve for fatigue life prediction. The research question that encapsulates this problem is the following:

How do repetitive low-velocity impact loads affect the failure modes and impact fatigue characteristics of composite sandwich structures used in high-speed crafts in low ice conditions?

3.2 Sub questions

The answer to the main question is developed by answering a few sub questions first, which will help to develop the basis for the conclusion. These questions incorporate the main failure characteristics of the material to low velocity impacts, the construction of the S-N diagram, determination of residual strength and damage accumulation and at last a life prediction model.

- What are the primary failure modes observed in composite sandwich structures under repetitive low-velocity impact loads?
- How can the S-N curve for quasi-isotropic carbon fibre reinforced epoxy be experimentally constructed?
- In what way can the obtained experimental data and existing literature on residual strength and damage accumulation be used to estimate the residual strength of the composite sandwich structure?
- How can the analysis of experimental data and existing literature be translated into actionable design recommendations to enhance the structural integrity of the vessel hull?

3.3 Overview of key elements in this research

Figure 3.1 provides an overview of the key elements and their dependencies within this research. It starts with the HSC and its environmental and structural requirements, which influence the impact loads and material type. These impact loads are exerted on the hull, which in turn affect the impact fatigue characteristics. These characteristics are important for the development of the S-N curve, assessing the failure modes, and predicting the residual strength and stiffness. Ultimately, this process leads to design recommendations aimed at enhancing the structural integrity of the HSC operating in low ice conditions.

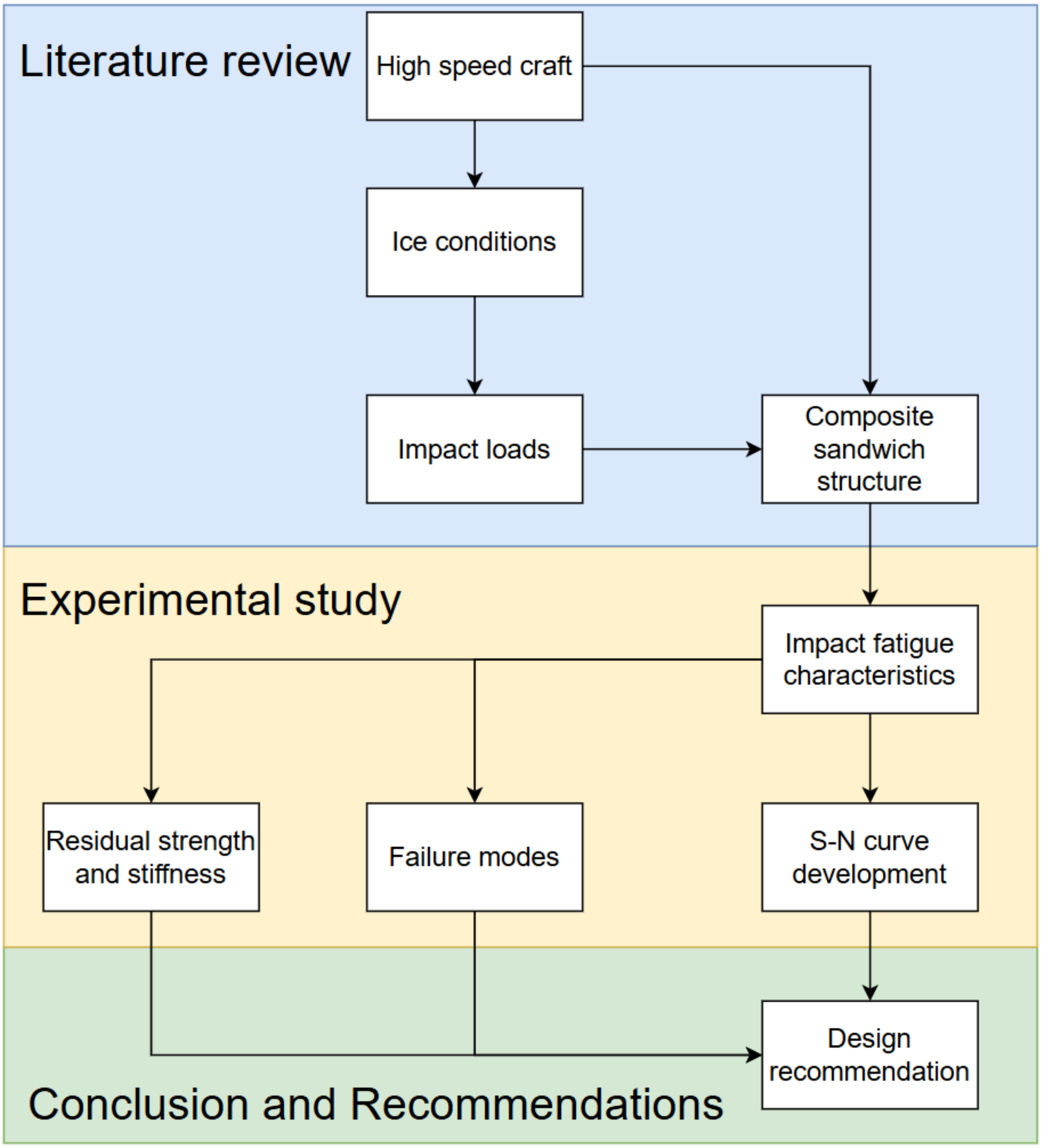

Figure 3.1: Overview key elements of this research shown in a block diagram

4 Methods and approach

4.1 Setup drop weight impact tower

Figure 4.1: Dynatub drop weight impact tower setup used at the facilities of UTwente

4.1.1 Description setup

The drop weight impact test method involves raising an impactor to the desired height and then releasing it, resulting in the impactor colliding with the test specimen. The Dynatub 8250 from the facilities of the university of Twente was used in this research and is shown in Figure 4.1 The test is executed according to the ASTM D7136/D7136M [54].

- The standard dimension for the test specimen is 150 mm x 100 mm x 4-6 mm.
- The impactor shall have a mass of 6.0 ±0.25 kg and shall have a smooth hemispherical striker tip with a diameter of 6 ± 0.1 mm and a hardness of 60 to 62 HRC.
- A force indicator will be used to record the force-time history. The force indicator shall be positioned such that at least 95 % of the impactor mass is located above it.
- The impact support will be a plate of at least 20 mm thickness, constructed from steel or aluminium. The cut out of the plate shall be 75 mm x 125 mm. The guiding pins must be placed to ensure the specimen is centered over the cut-out. Use four clamps to secure the specimen during the impact. The clamps must have a holding capacity of at least 1100 N..

4.1.2 Parameter determination

The impact energy of the drop can be calculated with the following equation:

$$E_{pot} = C_e h \tag{39}$$

Where E_{pot} is the potential energy, C_E is a specified ratio of impact energy to specimen thickness (6.7 J/mm), h is the thickness of the specimen. The drop height can be calculated with the following equation

$$H = \frac{E}{m_d g} \tag{40}$$

Where H is the drop height, m_d is the mass of the impactor and g is the gravitational constant

4.1.3 Material configuration

There will be two material type configurations used in this research, a standard configuration (REG) and a configuration with an additional woven E-glass layer for abrasive resistance(SAC). The standard configuration is a quasi-isotropic carbon epoxy composite lay-up, and the other lay-up will have an extra layer of woven E-glass on top. This configuration is the top sheet of the sandwich structure used in the hull of the vessel. Also the full sandwich structure will be tested to compare the results of the top sheet and the full sandwich.

4.1.4 Test matrix

The specimens will be tested on different impact energy levels to determine their number of cycles till failure (N). Initially, specimens will be subjected to the maximum energy level, followed by subsequent tests at 90% and 80% of this maximum and a fourth energy level, determined during testing. For precision purposes, every test will be repeated 3 times.

Table 11: Test matrix drop weight impact tower setup

Test Matrix	**Number of Tests**
Energy level max	3 tests
x% of Energy level	3 tests

4.1.5 Experimental design

The test procedure is stated below:

1. Specimen Preparation: Begin by preparing the target specimens according to the desired material and geometry specifications. Ensure that the specimens are homogeneous and free from defects that could influence the test results. In this research the samples were prepared by Damen shipyards and cut to specimen specifications.
2. Instrumentation Setup: Set up the drop weight impact tower, including the release mechanism for the weight and the target mounting apparatus. Calibrate any sensors or measurement devices used to capture impact force. In this research, a KISTLER force sensor (type 9011C) was used with a sensitivity of -4.212 pC/N.
3. Testing Procedure:
    (a) Place the target specimen in the designated position beneath the drop weight.
    (b) Adjust the drop height to the desired level for each test condition.
    (c) Release the weight, allowing it to fall freely onto the target specimen, generating an impact.

(d) Measure and record the impact force exerted on the specimen using appropriate sensors or instrumentation.

(e) Assess the damage extent on the specimen through visual inspection.

4.1.6 Data analysis

The impact force will be measured as a function of time using a load cell. The load cell directly measures the force over time. The software then processes this data to create four different plots: force vs. time, force vs. displacement, displacement vs. time, and velocity vs. time. These plots provide the necessary data, which is then used to calculate the absorbed energy. Also, the mean, deviation, and coefficient of variance will be calculated for each test.

The velocity vs time curve will be created using the equation below, using numerical integration of the force versus time data. The numerical integration will be performed using the trapezoidal rule, and the time step of the numerical integration must be equal to the time step of the sample data.

$$v(t) = v_i + gt - \int_0^t \frac{F(t)}{m}\,dt \tag{41}$$

Where v is the impactor velocity, v_i is the initial velocity, t is the time during the test ($t = 0$ at initial contact between impactor and specimen), and F is the measured impactor contact force.

The displacement vs time curve will be created using the equation below, using numerical integration of the force versus time data.

$$\delta(t) = \delta_i + v_i t + \frac{gt^2}{2} - \int_0^t \left(\int_0^t \frac{F(t)}{m}\,dt \right) dt \tag{42}$$

Where δ is the impactor displacement and δ_i is the initial impactor displacement at $t = 0$.

The absorbed energy vs time curve will be calculated with the following equation:

$$E_a(t) = \frac{m(v_i^2 - v(t)^2)}{2} + mg\delta(t) \tag{43}$$

Where E_a is the absorbed energy.

To calculate the mean value, the standard deviation for the parameters of each test specimen, the following equations will be used. The parameters that will be stated in the report are the contact force and the impact energy.

$$\bar{x} = \sum_{i=0}^{n_{sp}} \frac{x_i}{n_{sp}} \tag{44}$$

$$S_{n-1} = \sqrt{\frac{\sum_{i=0}^{n_{sp}} x_i^2 - n_{sp}\bar{x}^2}{n_{sp} - 1}} \tag{45}$$

$$\tag{46}$$

Where $\bar{x}$ is the sample mean, S_{n-1} is the sample standard deviation, n_{sp} is the number of specimens, and x_i is the measured parameter.

4.2 Setup air soft gun impact test

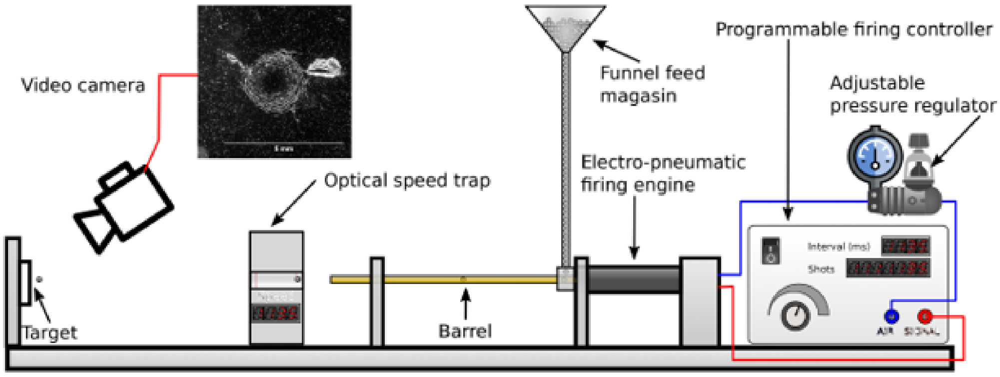

Figure 4.2: Schematic overview SPIFT[42]

4.2.1 Description setup

Table 12: Summary of commercial parts and FCU input parameters for the SPIFT setup

Part/Parameter	**HPA Engine**	**Barrel**	**Hop-up System**	**Chronograph**	**Arduino**	**dP (ms)**	**dN (ms)**	**dr (ms)**
Name/Value	Polarstar Fusion V2	Orga Magnus HD	Maxx CNC M4P PRO	Air Chrony MK3	Arduino Uno R4	17	26	25

The gas gun impact setup, shown in Figure 4.2, is a test method using compressed air and air-soft equipment to shoot small pellets at the specimens to recreate impacts with a significant lower impact energy. The test is not executed according to any ASTM standards, but it is a test setup designed and made within this research. The setup is based on an existing setup from the PhD thesis of Nicolai Johansen [42]. In this research, the setup of a single point impact fatigue test (SPIFT) was made and a summary of commercial parts used and parameter settings can be found in Table 12.

The setup is based around the commercially available high pressure air (HPA) airsoft firing engine. This HPA fire engine uses electro-pneumatic firing to shoot 6 mm diameter plastic pellets. The firing speed of this HPA engine ranges from 60-200 m/s, and it can shoot around 30 pellets per second. This velocity of the pellet is controlled by the air pressure that can be changed according to preference by a pressure regulator. In this research, the Polarstar fusion engine V2 will be used, as the electronics needed to control the solenoids and timing are already included.

The HPA engine nozzle is connected to the hop up system and inner barrel by a pressed fit. The hop up system ensures a better accuracy and range to the pellets, but most important it is a connection part for the inner barrel, nozzle and for this setup the funnel (normally the magazine in airsoft). The funnel feeds the pellet in the hop up chamber, the nozzle shoots the pellet in the inner barrel. For this research, a Maxx Model CNC Hop up Chamber M4P PRO (blue version) was used, as they are designed for HPA systems and particularly for the polarstar HPA nozzles. The inner barrel that is used is the Orga Magnus HD 6.13 mm. This inner barrel is slightly bigger than the standard inner barrel diameter of 6.03 mm. For this research this has a couple of benefits, the first one is that the manufacturing tolerances exceed the diameter of 6.03. This means that the pellet could not fire or get stuck at the beginning of the barrel. Another benefit is that a higher diameter also lowers the outlet velocity, but increases the accuracy. In this research, a lower velocity is more beneficial to recreate the lower impact energy.

The trigger will be bypassed and controlled by an Arduino uno R4 maxima. In this electrical circuit of the motor, there is also an FCU from Polarstar connected. In the FCU delivered with the HPA engine, a couple of parameters can be changed. The most import parameters for this research are the fire mode, the fire rate, poppet dwell(dP), nozzle dwell(dN) and return to battery delay(dr). The fire mode will be set to semi-automatic mode. The semi-automatic mode lets the Arduino count the number of signals sent to the HPA. With the use of semi-automatic mode, the fire rate can be maximized at 10 shots per second. The fire rate that will be used for this research will be 4 shots per second, this is the fire rate where the feeding of the pellets happens consistent without feeding issues. The other 3 settings are controlling the nozzle and the time air is released to the nozzle. The dP is the setting that controls the gas volume released through the nozzle, the higher this value the longer gas is allowed to flow. A fist rule in airsoft is that the longer the barrel the higher this value, the standard value for this setting is 21 ms. In this research a short barrel will be used so this value will be slightly decreased to match this short barrel. The dN is the setting which determines how long the nozzle is held back. This setting will be determined by trial and error by looking at the feeding of the pellets, if there are double feedings the setting should be lowered and if there are no feedings this setting should be increased. The dr is the setting that determines how long to wait for the nozzle to return forward while chambering the next pellet. This setting should be left at default, 22 ms, and only changed if proper feeding cannot be reached with changing the dN. The values for the settings were determined at dP is 17 ms, dN is 26 ms, dr is 25 ms.

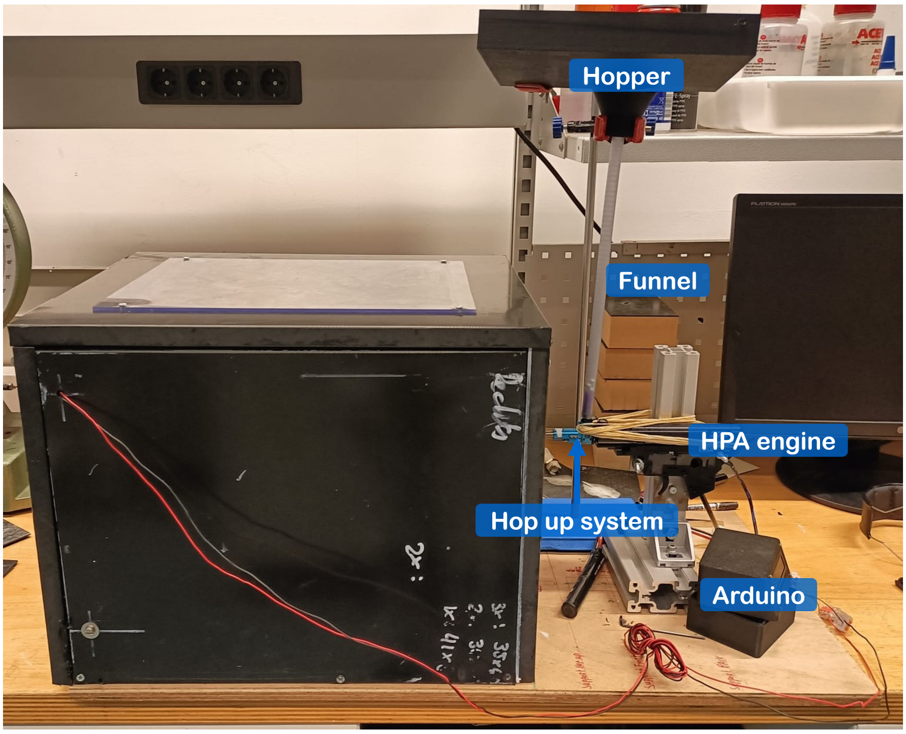

Figure 4.3: Front view SPIFT setup

The exit velocity of the pellet from the inner barrel will be measured with a chronograph, the Air

Chrony MK3. This chronograph measures with an error below 0.14 m/s and the data can be read onto a laptop or PC with the use of a USB cable. The chronograph can store 250 shots in its internal memory. This means that a relation between the inlet pressure and the exit velocity should be determined before the material testing will be done. This relation can be used to determine the impact energy used in the material tests.

The pellets are fed into the hop up chamber by a funnel with a hopper attached to it. A special plate will be 3D printed to create a smooth feeding of the pellets 1 by 1 into the hopper and funnel. This ensures that the pellets do not get stuck in the hopper and address other feeding issues. Figure 4.3 shows the final test setup.

4.2.2 Parameter determination

The exit velocity of the ball depends on a couple of factors, the length of the barrel, the pressure of the compressed air, the mass of the ball and at last also the size of the nozzle. The only factor that will be changed in this research will be the pressure of the compressed air. The relation between the pressure and the exit velocity can be measured with the chronograph, and these measurements will give the exit velocity. The data will then be fitted with a square root relation, and this fit curve will be used to determine the kinetic energy of the pellet [55]. The reason for fitting the data with a square root relation is related to Bernoulli's equation, which describes the conservation of energy in fluid flow. According to Bernoulli's principle [56], the pressure difference in a fluid system is related to the kinetic energy per unit volume of the fluid. Specifically:

$$P + \frac{1}{2}\rho v^2 + \rho g h = \text{constant} \tag{47}$$

If we neglect gravitational effects and assume the fluid starts from rest, the equation simplifies to:

$$P \propto \frac{1}{2}\rho v^2 \tag{48}$$

Rearranging for velocity:

$$v \propto \sqrt{P} \tag{49}$$

Thus, the velocity is proportional to the square root of the pressure, which justifies the choice to fit the data with a square root relation [56].

4.2.3 Material configuration

The material configuration will be the same as in the drop weight impact tower test.

The material of the pellets will be steel and aluminium. The impact resistance of the metals will be sufficient that the damage on the pellets is neglectable, and thus they can be reused in the test setup. The weight of the pellets is 0.996 g for the steel pellets and 0.298 g for the aluminium pellets (mean of 100 pellets). Steel and aluminium are used because their damage mechanics are well understood and less complex compared to viscoelastic polymers. Additionally, the deformation of the pellets is a significant factor in the impact tests, and using steel and aluminium ensures consistent and predictable results.

4.2.4 Test matrix

The specimens will be tested on different impact energy levels to determine their amount of cycles till failure (N). The test matrix is shown in Table 13.

Table 13: Test matrix gas gun setup

Energy Level	**0.3N**	**0.5N**	**0.8N**	**N**
Min	3 tests	3 tests	3 tests	3 tests
...	3 tests	3 tests	3 tests	3 tests
Max	3 tests	3 tests	3 tests	3 tests

4.2.5 Experimental design

The test procedure for the chronograph speed test is stated below:

1. Instrumentation setup: Set up the chronograph in the right position in front of the barrel of the SPIFT gun. Set up the SPIFT by connecting the laptop and the Arduino. Set up the desired inlet pressure in the pressure regulator.
2. Testing procedure:
    (a) Clamp a target within the clamps
    (b) Adjust the inlet pressure to desired level
    (c) Shoot 100 pellets to the target with the use of the Python GUI
    (d) Detach the power and the compressed air to the HPA engine and read out the data from the chronograph with the laptop.

The test procedure for the SPIFT is stated below:

1. Specimen preparation: Begin by preparing the target specimens according to the desired material and geometry specifications. Ensure that the specimens are homogeneous and free from defects that could influence the test results.
2. Instrumentation setup: Set up the air soft gun set up by connecting the laptop and the Arduino. Set up the calculated inlet pressure and run the python code to start the testing GUI. Start the test in the GUI and send the command for the fire rate and amount of shots.
3. Testing procedure
    (a) Clamp the target specimen within the clamps
    (b) Adjust the test parameters in python GUI and pressure regulator
    (c) Start shooting in the GUI and shoot the air-soft pellets to the target.
    (d) Shoot with use of increments to the predicted amount till failure and between every increment asses the damage extent on the specimen through visual inspection and/or use of microscope.

4.2.6 Data analysis

The data from the chronograph will be used to calculate the average value and the standard deviation, as in subsubsection 4.1.6. The results will be used to fit a relation for the inlet pressure and outlet pressure. This fit is a square root relation and can be seen in Equation 50.[55]

$$y = a\sqrt{x} + b \tag{50}$$

The results from the "gas gun" setup can be used to determine the number of cycles till failure by visual inspection, and also prepare specimens for the CAI test setup. The impact energy of the air soft setup will be calculated with the kinetic energy equation.

$$E = \frac{1}{2}mv^2 \tag{51}$$

The magnitude of N and the absorbed energy can be used to determine the E-N curve. This curve can be fitted with the power law method developed by Basquin [50]. This relation can be seen in Equation 52 with fitting parameters A and m. Normalization of the energy for comparison between different material lay-ups is done by normalizing over the thickness, according to the research of Nettles. [57].

$$E = A \cdot N^m \tag{52}$$

For each series of tests, the average value, and standard deviation is calculated for the number of cycles till failure. This calculation is performed in the same way as in subsubsection 4.1.6. For the curves fits a 95 % confidence interval will be calculated. The 95 % confidence interval for m is calculated with the following equation.

$$m \pm t_{\alpha/2,dof} \cdot S_{n-1} \tag{53}$$

where $t_{\alpha/2,dof}$ is the critical t-value for the 95 % confidence interval and the given degrees of freedom and S_{n-1} is the standard deviation. This calculation will also be used for other fits like the speed test fit.

4.3 Setup Compression after impact test

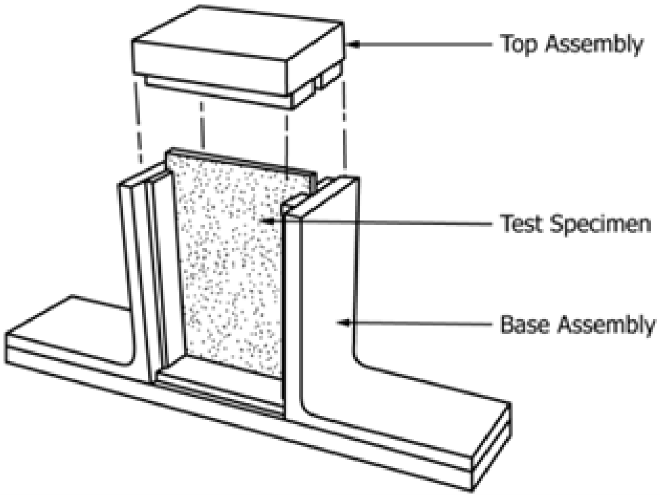

Figure 4.4: Schematic overview compression after impact

4.3.1 Description setup

The compression after impact test involves subjecting a composite plate damaged by an impacting event to a compressive force to determine the residual strength. The test is executed according to the ASTM D7137/D7137M – 17 [43].

- The standard dimension for the test specimen is 150 mm x 100 mm x 4-6 mm.
- The specimen is damaged by an application of an out-of-plane drop weight impact in accordance to ASTM D7136/D7136M [54].
- The specimen is installed in a support fixture that is aligned to minimize loading eccentricities and induced specimen bending. The fixture consists of one baseplate, two base slide plates, two angles, four side plates, one top plate, and two top slide plates. Detailed dimensions can be found in the ASTM D7137/D7137M – 17 [43].
- The force-sensing device on the testing machine needs to show the total force applied to the test specimen.

4.3.2 Material configuration

The material configuration will be the same as in the drop weight impact tower test.

4.3.3 Test matrix

The impacted specimens will be tested on residual compressive stress at different fractions of the number of cycles till failure. The fraction of N that the specimens are impacted on 0N; 0.3 N; 0.5 N ; 0.8 N; 1.0N. For precision purposes, every test will be repeated 3 times.

Table 14: Test matrix CAI test setup

Energy Level	**0N**	**0.3N**	**0.5N**	**0.8N**	**1.0N**
Min	3 tests	3 tests	3 tests	3 tests	3 tests
...	3 tests	3 tests	3 tests	3 tests	3 tests
Max	3 tests	3 tests	3 tests	3 tests	3 tests

4.3.4 Experimental design

The test procedure is stated below:

1. Specimen Preparation: Prepare the specimens for the CAI test, ensuring consistency in material properties and geometry across samples. Prepare the specimens to the desired damage fraction in a controlled manner.
2. Damage assessment: Asses the damage to the specimen with optical microscopy.
3. Instrumentation Setup: Set up the compression testing apparatus, including the loading frame, grips or fixtures for specimen fixation, and instrumentation for data collection.
4. Testing Procedure:
    (a) Secure the impacted specimen in the compression testing apparatus, ensuring proper alignment and fixation.

(b) Apply compressive load to the specimen at a constant rate or displacement, simulating the structural response under compression after impact.

(c) Measure and record the applied load and corresponding deformation or displacement of the specimen throughout the compression test.

(d) Assess the residual strength and extent of damage in the specimen based on the load-displacement curve and post-test examination.

4.3.5 Data analysis

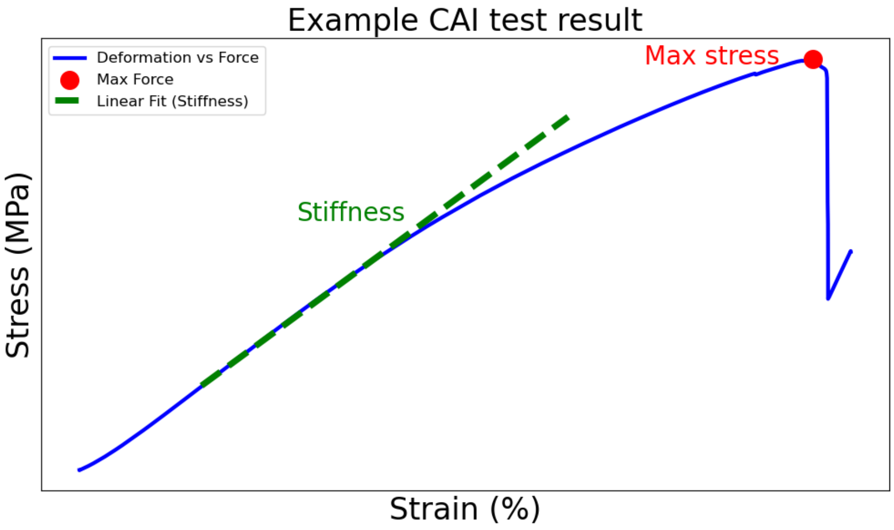

Figure 4.5: Schematic overview example result CAI test

In Figure 4.5 a schematic overview of a result curve from the CAI test is plotted. The results from the CAI test can be used to determine two important material properties. The residual compressive strength and the effective compressive modulus. The residual compressive strength will also be used in Shokrieh's [53] prediction model to predict the residual strength. The residual compressive strength can be calculated with the following formula:

$$\sigma_{CAI} = \frac{P_{max}}{A} \tag{54}$$

Where σ_{CAI} is the ultimate compressive residual strength, P_{max} is the maximum force prior to failure, A is the cross-sectional area.

The effective compressive modulus is the compressive stiffness and is calculated by deriving the slope of the linear region of the curve, can be seen in Figure 4.5. This slope is derived by linear regression from the stress data points between a strain range.

For each series of tests, the average value, and standard deviation is calculated for the ultimate compressive residual strength. This calculation is performed in the same way as in subsubsection 4.1.6.

The Shokrieh model is explained in subsubsection 2.10.2. The model can be seen in Equation 55 and the data from the test setups will be used to calculate the fitting parameters and to predict the residual strength.

$$(\frac{X_r - \sigma_{max}}{X - \sigma_{max}})^{\alpha} = 1 - (\frac{log(n) - log(0.25)}{log(N) - log(0.25)})^{\beta} \tag{55}$$

5 Results

Figure 5.1 presents an E-N curve illustrating the relationship between impact energy and the number of impacts for the test material under two different test setups: the drop weight impact test (DWIT) and the air soft impact test. The curve is fitted using the Basquin fit [50], showing a decrease in energy as the number of impacts increases. The shaded regions in the figure represent data from each specific test configuration. The DWIT data, shown in the green-shaded area, cover a range of higher energies (4 - 15 J) and lower impact counts (1 - 100 impacts), while the air soft impact test data, shown in the blue-shaded area, correspond to lower energy levels (0.5 - 2 J) over a much wider range of impacts (100 - 10^6 impacts). The yellow-shaded area represents the data points from the compression after impact test (CAI), which measures residual strength and stiffness at different fractions of N. This section presents the results from the different test setups and combines them into a final E-N curve for both test material lay-ups.

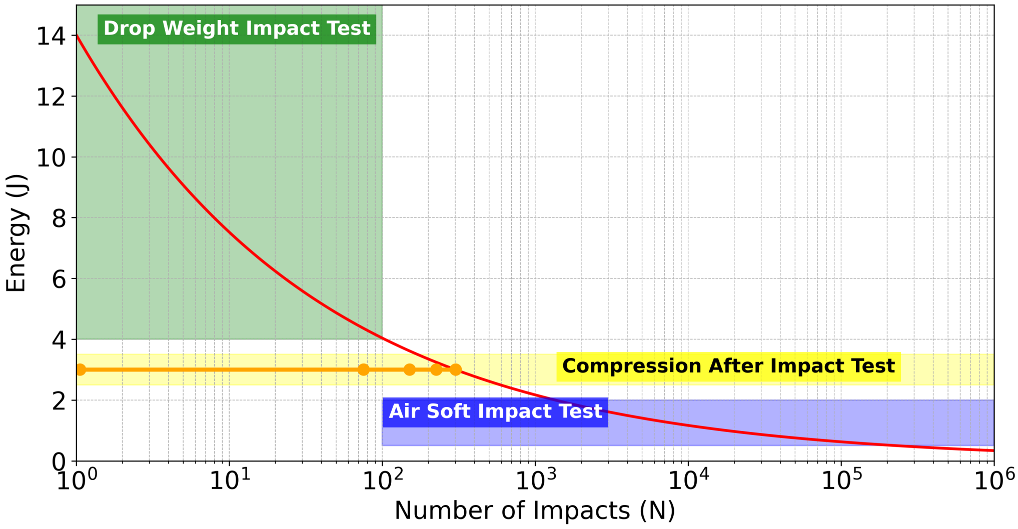

Figure 5.1: Overview test setups data in E-N curve

5.1 Drop weight impact tower results

In the first part of the testing phase, the DWIT tests are conducted. Data from the force sensor, which is attached to the impact tube, are used to plot three different curves that provide insights into the impact characteristics of the test material. The number of impacts until failure at each tested energy level is then plotted in an E-N curve. When combined with the SPIFT results, this will create the final E-N curve for the specific test material lay-up.

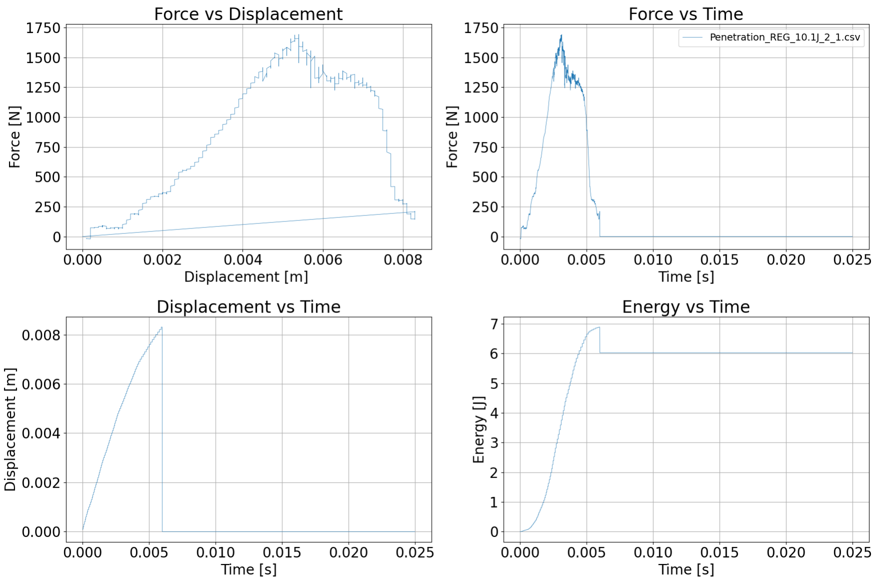

Figure 5.2: Measured data of the DWIT test for a sample fully penetrated at 1 impact with a fracture energy of 7.3J

5.1.1 Results till failure REG material

In Figure 5.2 an overview of the results for a penetration test with one impact is shown. In this curve the outline of the curve is shown nicely. For multiple impacts the shape of the force displacement curve will be thinner en increasingly get thicker over the number of impacts. This is because the absorbed energy of the test is expected to increase over the number of impacts. The force time curve shows a curve that is far from symmetrical. In the data curves for multiple impacts this curve starts with a more symmetrical shape and over the course of impacts this curve will show resonance at the top of the curve, related to an increase in absorbed energy. This expected behavior is shown in Figure 5.3

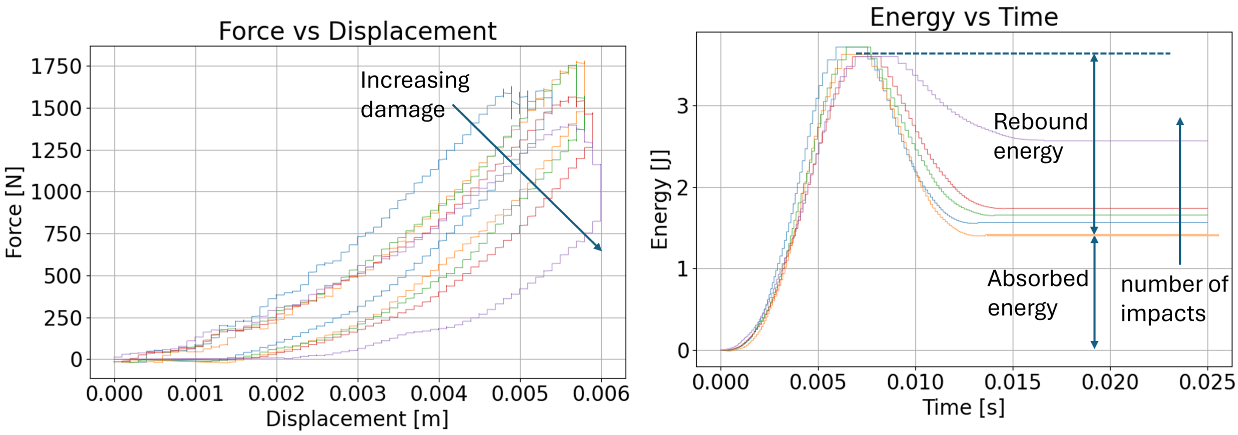

Figure 5.3: Expected behavior DWIT test results

The results of an example penetration test in the DWIT (4.3J) are shown in Figure 5.4. The plots exhibit the expected behaviour, with increasing displacement and decreasing maximum force as the number of impacts increases.

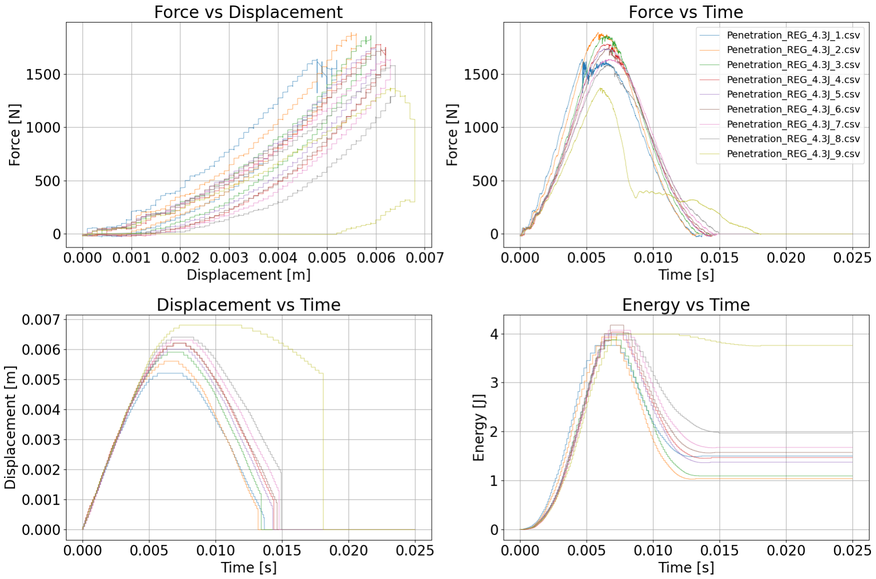

Figure 5.4: Measured data of the DWIT test for 4.3 J, first plot is force-displacement curve, second curve is force-time curve, third plot is displacement-time curve and the fourth one is the energy-time curve

This relationship also affects the absorbed energy. The increasing trend of absorbed energy with the number of impacts can be seen in Figure 5.5. This figure also shows example plots of the relationship between maximum force, maximum displacement, rebound energy, and the number of impacts. The relation between the data points demonstrates that the first few impacts exhibit lower maximum force and higher absorbed energy, which does not align with the expected behaviour. Figure 5.5 is included to highlight these irregularities, as it is not clearly visible in the other plots above. This behaviour will be further elaborated on in subsection 6.5

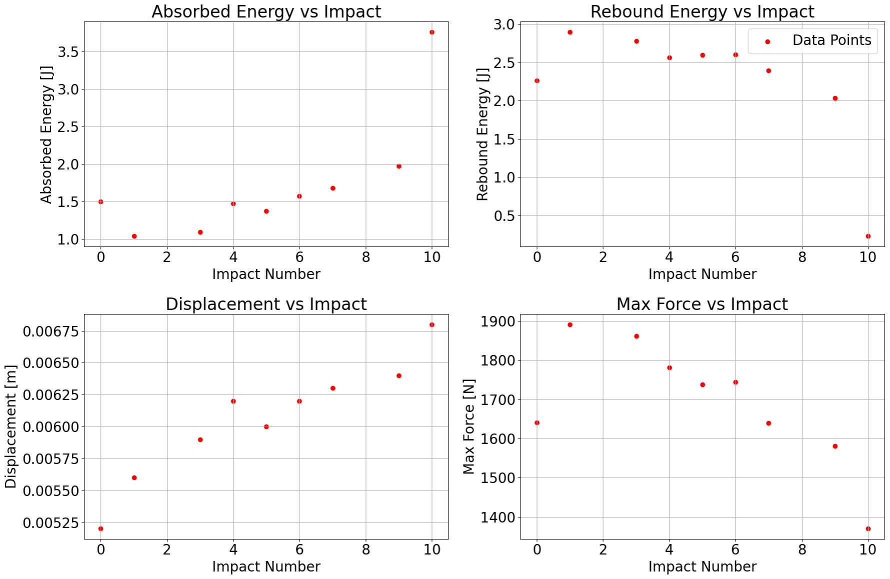

Figure 5.5: Relation curves of the absorbed energy, rebound energy, displacement, and maximum force against the impact number

In Figure 5.6, an image of the DWIT results is shown, displaying an energy versus number of impacts curve with the fitted relationship. This fitted relationship is based on the results of both the DWIT and the SPIFT results. The data points representing the number of impacts until penetration are shown, along with their mean and standard deviation.

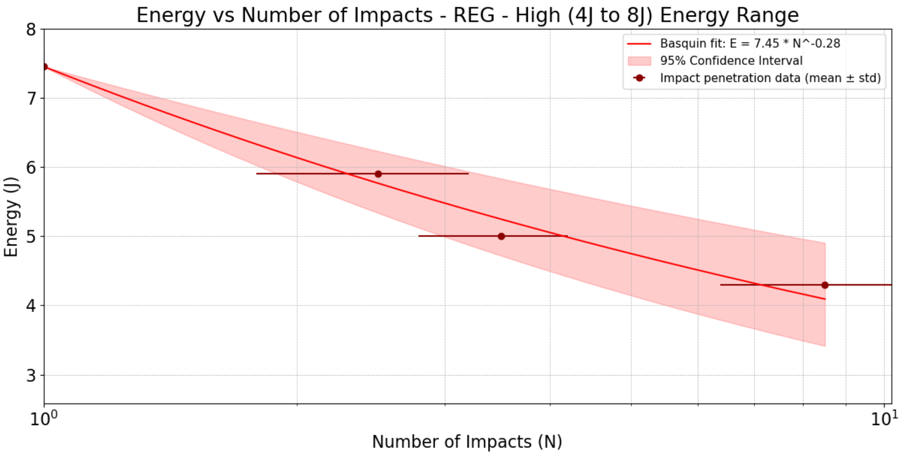

Figure 5.6: Results DWIT for the regular material: Energy vs number of impacts till penetration

5.1.2 Results till failure SAC material

In Figure 5.7, the number of impacts versus impact energy for the DWIT test on the SAC material is shown, along with the mean and standard deviation. The Basquin fit is used to create a curve for the results. The data points fall neatly within the 95% confidence interval, and for the 12.0 J and 4.9 J energy levels, the data spread is very small.

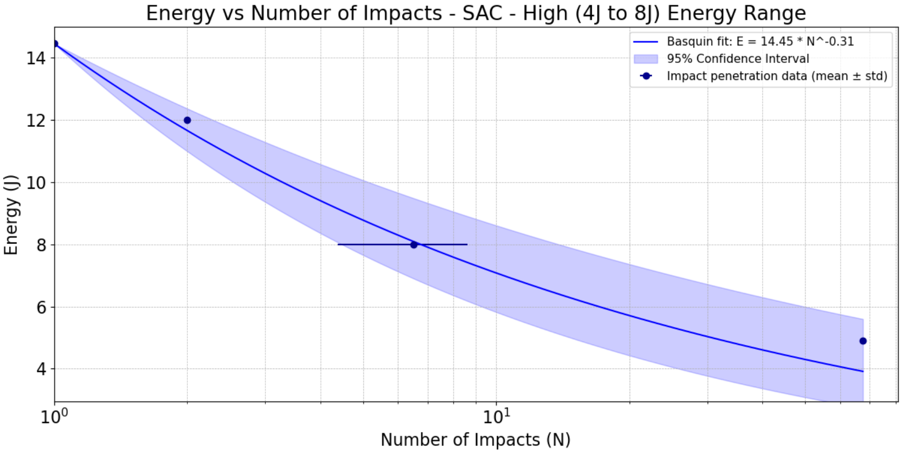

Figure 5.7: Results DWIT for the SAC material: Energy vs number of impacts till penetration

5.2 Air soft impact test results

The SPIFT results are used to obtain the data for the low energy part of the E-N curve. First, the relationship between the inlet pressure and exit velocity must be measured for both pellet material types. This relationship can then be applied in the SPIFT to determine the number of impacts until penetration, completing the E-N curve.

5.2.1 Speed test results

The velocity of the pellet as a function of inlet pressure was measured by firing one hundred pellets through the chronograph. The mean and standard deviation were calculated and plotted against the inlet pressure, as shown in Figure 5.8. These curve fits are then used to calculate the kinetic energy of the impact for the SPIFTs.

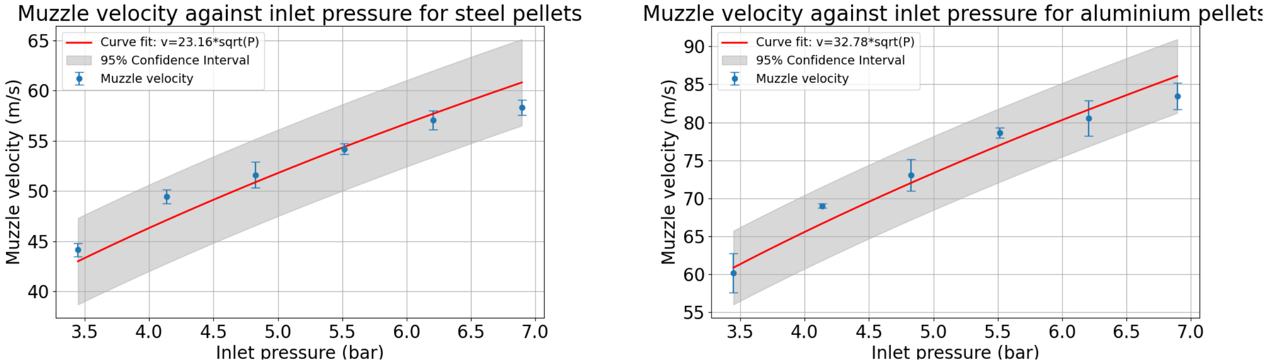

(a) Inlet pressure vs muzzle velocity steel pellets (b) Inlet pressure vs muzzle velocity aluminium pellets

Figure 5.8: Inlet pressure against muzzle velocity plots

5.2.2 Results till failure REG material

In the SPIFT, five energy levels were tested until penetration. Three energy levels were tested with steel pellets, and two energy levels with aluminium pellets. The test was performed on the regular material. The results are shown in Figure 5.9.

The results from the SPIFT follow the Basquin curve fit, based on both DWIT and SPIFT results, closely. The two lower energy levels, tested with aluminium pellets, require fewer impacts to failure and fall outside the bounds of the 95% confidence interval.

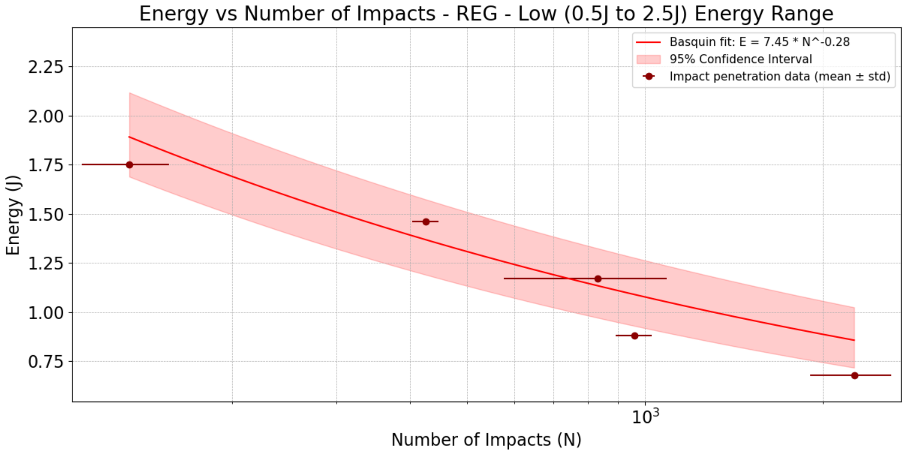

Figure 5.9: Results air soft impact test for the regular material: Energy vs number of impacts till penetration

5.2.3 Results till failure SAC material

In Figure 5.10, the penetration results of the SPIFT are shown. The SPIFT do not match the curve fit well, and the two lower energy levels fall outside the 95% confidence interval. These energy levels were tested with aluminium pellets and show a significantly lower number of impacts than the curve fit predicts.

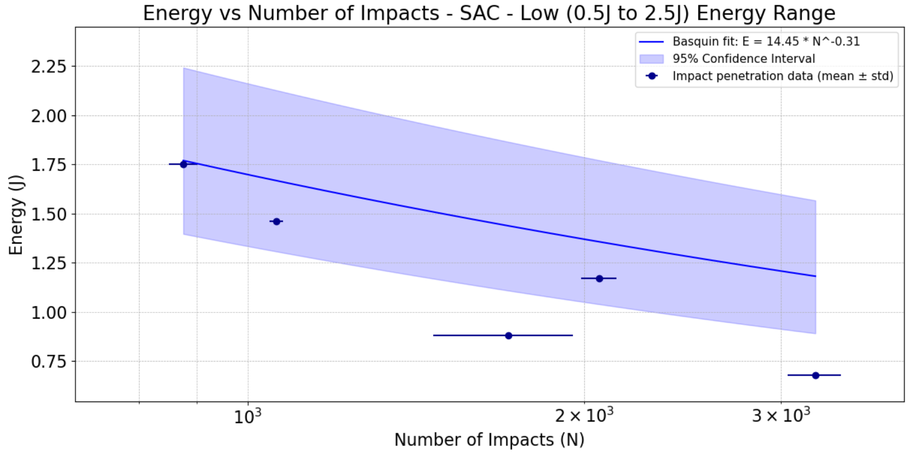

Figure 5.10: Results air soft impact test for the SAC material: Energy vs number of impacts till penetration

5.3 Energy versus amount impacts till failure curves

In this section, the full E-N curves for both material lay-ups, the comparison of the full sandwich to the REG results, and the E-N curves normalized over the thickness are presented.

5.3.1 E-N curve REG with full sandwich results

In Figure 5.11, the results of the full sandwich (blue) are shown, plotted with the E-N curve fit and data points of the REG material. The figure demonstrates that the sandwich data fall within the 95% confidence interval of the REG curve fit. These results support the expectation that the difference between testing only the top layer or the full sandwich would be relatively small.

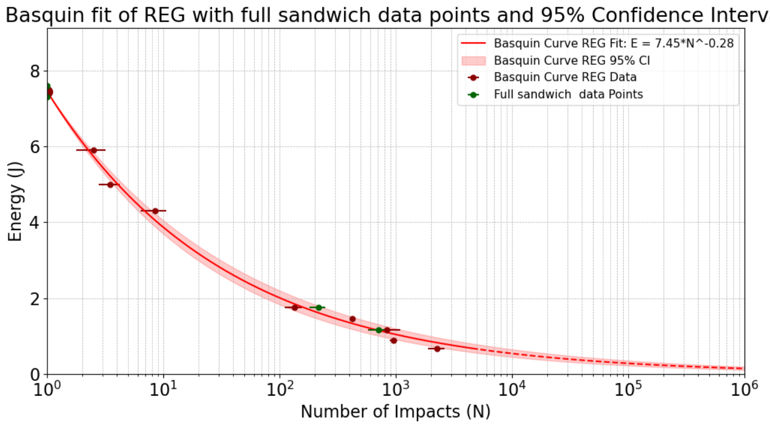

Figure 5.11: E-N curve of the REG material with the results of the impact testing of the full sandwich

5.3.2 E-N Curves for Material Lay-ups

In Figure 5.12, the combined results of the DWIT and SPIFT tests for both material types are shown in an E-N curve, fitted with their 95% confidence intervals. The figure shows that both E-N relationships follow a similar slope, but the material lay-up with the sacrificial layer has a higher starting number of impacts.

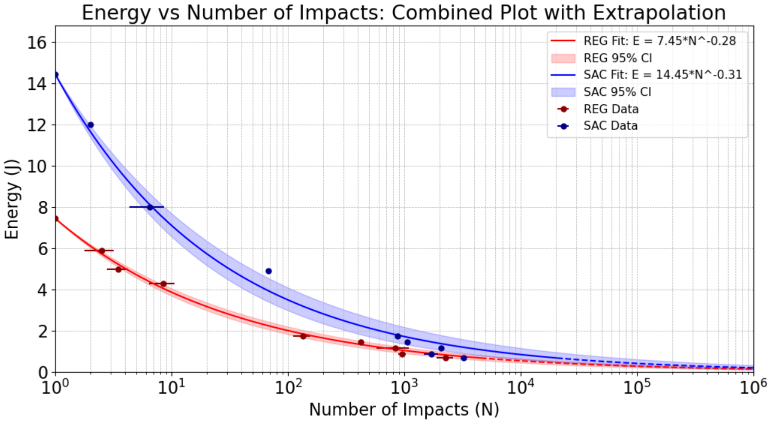

Figure 5.12: Comparison plot of the E-N curves for both material types

5.3.3 Normalized E-N Curves on Thickness

To standardize the comparison between the two material types, the E-N curves were normalized by thickness, as is common in the literature [57]. In Figure 5.13, the normalized E-N curves for both the REG and SAC material types are presented. The results indicate that the additional sacrificial layer significantly influences the high-energy region of the curve, where the number of impacts until failure is notably higher for the SAC material. However, in the lower-energy region, the sacrificial layer does not contribute to an increase in the number of impacts until failure, with both material types exhibiting similar behavior. This suggests that the additional layer primarily enhances the material's performance under high-energy impacts, but has little effect in the lower-energy range.

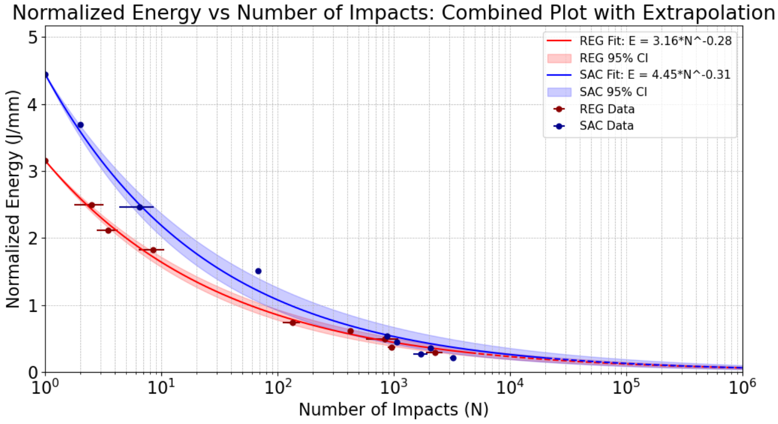

Figure 5.13: Comparison plot of the E-N curves normalized over the thickness for both material types

5.4 Compression after impact test results CAI

In this section, the results of the CAI tests are presented. During testing, five damage fractions per energy level were tested to obtain the force-displacement behaviour of the damaged samples. From these force-displacement curves, the residual strength and stiffness were calculated and are shown in the bar graphs in this section.

5.4.1 CAI Results for REG

In Figure 5.14, the residual strength and stiffness bar graphs for the REG material are shown. The figure reveals that, in general, no clear trend is visible. The expectation was that a slight decreasing trend would be observed. The results for the undamaged and fully damaged samples show a slight decrease in strength and stiffness.

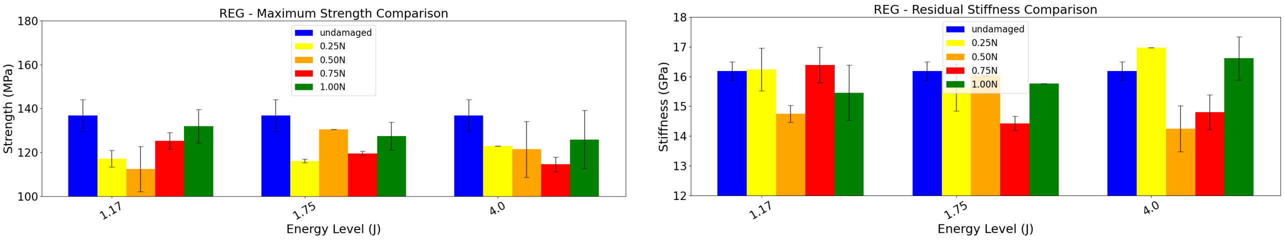

Figure 5.14: Bar graphs comparison residual strength and stiffness for the SAC material type with mean and standard deviation

Table 15 presents the mean strength and stiffness values for the REG material at 1.00 N and an undamaged damage fraction, along with the differences between these properties. The results show only a non-significant decrease in strength. While a negative difference in stiffness is observed, this, along with the other stiffness differences, is also non-significant. Consequently, these findings are not emphasized further, as they do not have meaningful implications for subsequent discussions.

Energy (J)	$E_{1.00N}$ (GPa)	$\sigma_{1.00N}$ (MPa)	E_{0N} (GPa)	σ_{0N} (MPa)	ΔE (GPa)	$\Delta\sigma$(MPa)
1.17	15.6	129.7	16.2	136.9	0.6	7.2
1.75	15.8	133.7	16.2	136.9	0.4	3.2
4.00	16.6	125.9	16.2	136.9	-0.4	11.0

Table 15: REG Data: Mean stiffness and strength values, undamaged values, and differences.

5.4.2 CAI results SAC

Figure 5.15, the residual strength and stiffness bar graphs for the SAC material are shown. The figure reveals a slight decreasing trend between the damage fractions for the lower energy levels (1.17 J and 1.75 J). The 0.75 N damage fraction for the 1.17 J energy level has no results, as the samples prepared for this test were fully penetrated at 0.75 N. For the high energy level (8.0 J), no trend is visible.

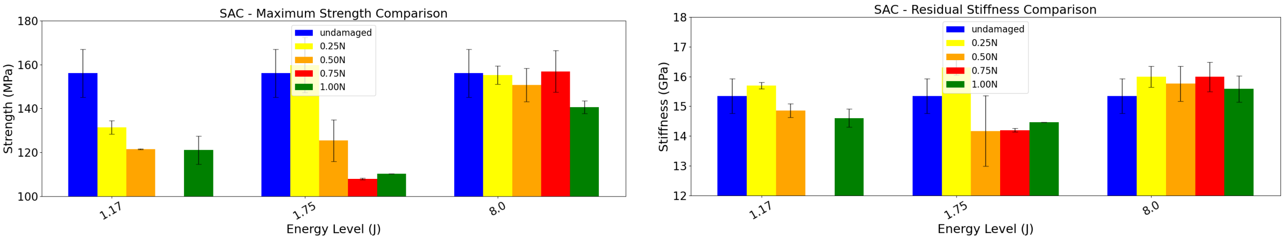

Figure 5.15: Bar graphs comparison residual strength and stiffness for the SAC material type with mean and standard deviation

In Table 16 presents the mean stiffness and strength values, along with the differences between fully penetrated and undamaged conditions. The results indicate that low-energy impacts cause a significant degradation in strength compared to high-energy impacts, while the differences in stiffness are non-significant.

Energy (J)	$E_{1.00N}$ (GPa)	$\sigma_{1.00N}$ (MPa)	E_{0N} (GPa)	σ_{0N} (MPa)	ΔE (GPa)	$\Delta\sigma$ (MPa)
1.17	14.6	121.0	15.3	156.1	0.7	35.1
1.75	14.5	110.3	15.3	156.1	0.8	45.8
8.00	15.6	140.7	15.3	156.1	-0.2	15.5

Table 16: SAC Data: Mean stiffness and strength values, undamaged values, and differences.

5.5 Microscopy pictures

In this research, samples with a damage fraction of 0.5N were cut to examine the surface of the layers for the delamination and fracture in the layers of the impact location. The same energy levels were examined as the CAI energy levels for both material lay-ups. The clearest difference in failure mode and delamination area was found in the examination of the REG 4.0J and the REG 1.75J. The pictures of the microscopy can be seen in Figure 5.16.

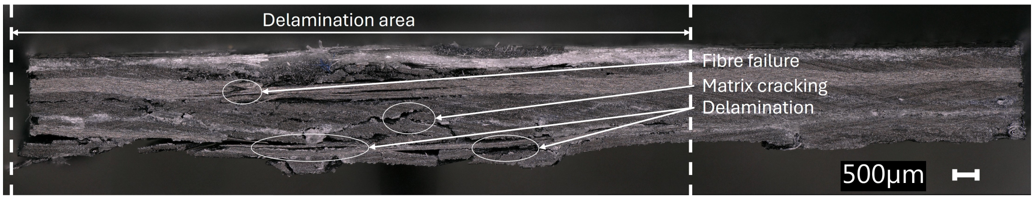

(a) REG 1.75J microcopy surface picture

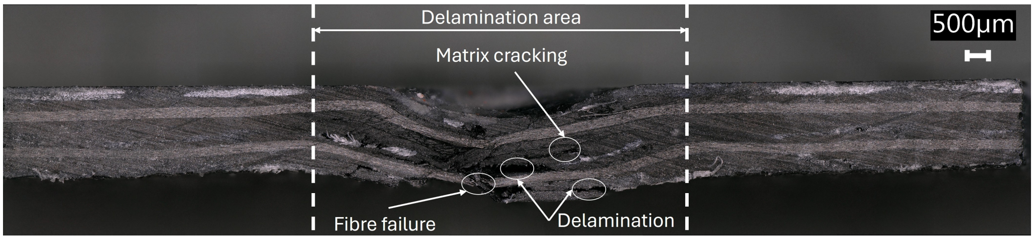

(b) REG 4.0J microscopy surface picture

Figure 5.16: Optical microscopy picture of the inside layers of the REG material for 1.75J and 4.0J and 0.5N damage fraction

In Figure 5.16b, the layers exhibit out-of-plane deformation, matrix cracking, fibre failure around the impact area, and some delamination between the layers. In contrast, Figure 5.16a shows no significant out-of-plane deformation, but the failure appears more complex, with extensive matrix and fibre damage. Notably, the delamination area around the impact location is larger for the 1.75J specimen, corresponding to the CAI results. The difference in strength between undamaged and fully penetrated specimens is significantly greater for lower-energy impacts than for high-energy impacts. Unlike the 4.0J specimen, the 1.75J specimen shows no out-of-plane deformation at the impact point; instead, the impact location appears eroded rather than indented.

6 Discussion

In this section, the experimental results are critically analysed in the context of the research objectives, methodological considerations, and existing literature. The goal is to evaluate the significance of the results, address discrepancies, and explain unexpected relations or patterns. In this research, a few key points need to be addressed, including issues with methodological validation, variability in results, and deviations from standardized testing protocols. Every key point will be discussed in this section by addressing the potential explanation and advice for future research.

6.1 Validation SPIFT results with DWIT tests

The use of two different test setups to create an E-N curve without overlapping and validating results raises questions about the validity and compatibility of these methods. The in-house developed SPIFT could have been validated by performing DWIT tests at lower energy levels, allowing a comparison of the number of impacts until failure and potential differences in failure mechanics. However, the experimental limitations of the DWIT make this approach impractical, as it would require significant manual labour to conduct hundreds of repeated impacts at the low energy levels achieved by the SPIFT. This was the reasoning behind constructing the SPIFT for a high frequency of impacts at low energy levels, making it a more feasible solution for studying composite lay-ups under impact fatigue.

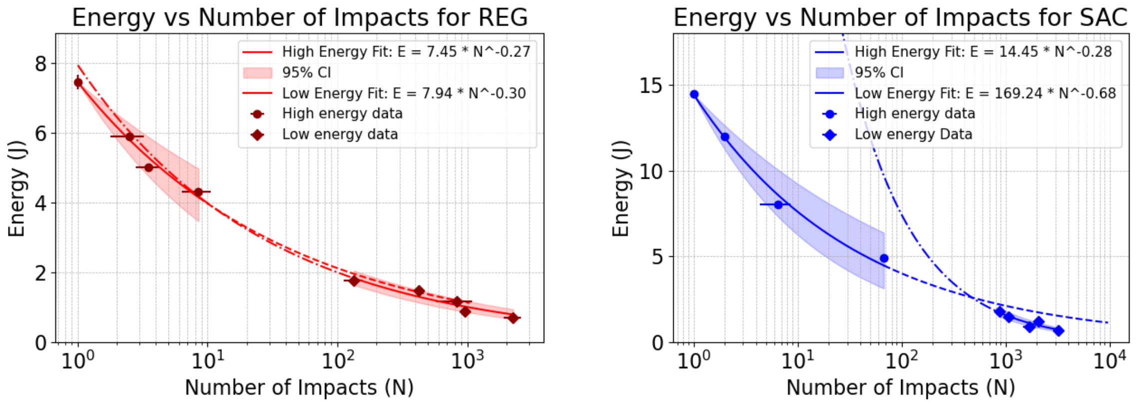

(a) Curve fit for both test setups REG material

(b) Curve fits for both test setups SAC material

Figure 6.1: Curve fit plots with 95% confidence intervals for both material types

In Figure 6.1, the fits for both test setups are shown, fitted to the tested energy levels without accounting for the transitional phase. While the REG fits show similar starting numbers and power law coefficients, the SAC fits display significant differences between lower and higher energy levels in both parameters.

Several factors may explain this discrepancy. First, as shown in subsection 5.5, the failure modes differ between high and low energy levels, suggesting that a transitional point or area likely exists within the untested energy range where failure mechanics shift. Additionally, the data points for the low-energy tests are limited, as failures with aluminium pellets occur after significantly fewer impacts, reducing the robustness of the fit. Lastly, the asymmetric lay-up of the SAC material may contribute to the observed differences in the fit.

To further investigate this, a new fit was performed excluding the aluminium results, yielding $E =$

$36.72 \cdot N^{-0.45}$. This fit shows a significant difference compared to the fit including aluminium results ($E = 169.24 \cdot N^{-0.68}$). The new fit is shown in Figure 6.2

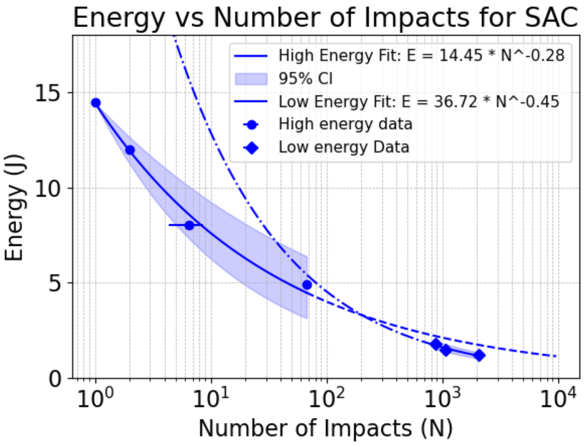

Figure 6.2: Curve fit plots for SAC (without aluminium results) with 95% confidence intervals

The exclusion of aluminium results demonstrates that the fits for low and high energy levels complement each other more closely, suggesting that the aluminium pellet failures were indeed skewing the fit due to their premature failure. This supports the argument that material response differences, rather than just failure point variability, contribute to the observed fit discrepancies.

Despite the constraints in directly comparing results, the resulting curve fit shows a smooth transition between the DWIT and SPIFT data, suggesting potential compatibility. This indicates that the SPIFT can effectively assess composite lay-ups for low-energy, high-frequency impacts and contributes to constructing the E-N curve for a better understanding of impact fatigue characteristics. Future research should focus on validating the comparability of these two setups by using materials that fail after only a few impacts at lower energy levels. Such studies would be a critical first step in further developing and standardizing the SPIFT.

6.2 CAI results

The Compression After Impact (CAI) results show no clear trend in residual strength and stiffness across the damage fraction (0N, 0.25N, 0.5N, 0.75N, and 1.0N). A slight decrease in both residual strength and stiffness can be observed between the undamaged state and the fully penetrated state for both material types. The expected relation is that the residual strength and stiffness would decrease with the increasing number of fatigue cycles.[45]

Table 17: Reinforcement/resin combined material properties provided by Damen Shipyards

Property	**Unit**	**E-Glass UD**	**Carbon UD**
rho	kg/m^3	1876	1510
nu$_{12}$	-	0.286	0.277
E_{xx}	GPa	36.321	116.018
E_{yy}	GPa	7.398	5.487
G_{xy}	GPa	3.382	3.583
$\sigma_{xx,t}$	MPa	981	1544.8
$\sigma_{xx,c}$	MPa	654	640.6
$\sigma_{yy,t}$	MPa	39	55
$\sigma_{yy,c}$	MPa	115	94.5
τ_{xy}	MPa	60.9	57.3

Comparing the analytical values for the stiffness of the undamaged specimens with the experimental values from the CAI tests, something quite interesting shows. The analytical values for the stiffness for both material types are calculated with the engineering properties of Table 17 as input of the classical laminate theory [58]. The following analytical values for the stiffness were calculated:

$$E_{REG} = 32.61\ GPa$$
$$E_{SAC} = 13.42\ GPa$$

Compared to the experimental values shown below, the value for the REG material is significantly lower than the analytical value, whereas the SAC material's value is within the range of the analytical value. The most important difference between the two materials, apart from the lay-up, is the difference in thickness. The REG material specimens have a mean thickness of 2.36 mm, while the SAC material has a mean thickness of 3.25 mm. This significant difference could mean that the REG material was more susceptible to out of plane deformations under the compressive loading during testing, resulting in a notable reduction in the experimental stiffness.

$$\begin{aligned} E_{REG.exp} &= 16.19 \pm 0.31\ GPa \\ E_{SAC.exp} &= 15.34 \pm 0.58\ GPa \end{aligned}$$

One possible explanation for the lack of a clear trend and the difference between analytical value and experimental value is the presence of varying failure modes across the damage fractions. In subsection 2.8 the different failure modes were discussed and shown in Figure 2.13. The different damage modes, such as notching, global and/or local buckling, or combinations of these modes, can dominate depending on the extent of the damage introduced by the impacts. Also, the failure modes can interact with each other, leading to complex behavior that deviates from a predictable trend.

Additionally, out-of-plane deformations introduced by the impact could significantly affect the residual strength and stiffness. These deformations might induce localized stress concentrations or changes in the load transfer mechanisms, potentially obscuring any trend associated solely with the damage fraction. Evaluating the extent of these deformations through additional measurements or simulations could provide more clarity.

Given the lack of a clear trend and the observed complexities, alternative approaches could be investigated to better characterize and predict the residual properties of the composite after impact.

The research of Sjöblom and Hwang [59] proposed the use of a steel anti-buckling support featuring a central hole designed to avoid interfering with the damage region. However, this design precludes the use of strain gauges. Additionally, the device requires narrow specimens with end tabs, which may lead to alterations in geometry after conducting the impact test. Sanchez-Saez et al. [60] introduced a CAI device that stabilizes the specimen using four anti-buckling plates positioned on both sides. These plates include cut-outs specifically designed to prevent interference with the damaged area. This device ensures that failure occurs within the affected region and has been used to determine the CAI strength of laminates with thicknesses ranging from 1.6 to 2.2 mm. The ESWNM department of Airbus Operations SL [61] developed a compression device equipped with horizontal rolls, which enhances the critical buckling load to facilitate testing of thinner specimens. This device incorporates lateral guides and rolls to prevent buckling during testing. The specimen is secured using screws, which eliminates the need for perfectly parallel edges during load application. However, drilling is required to attach the specimen to the clamping system.

Further research into one of these test alternatives of the CAI test is recommended for getting insights in the relation of the residual strength and stiffness and the damage fractions.

6.3 Deviations from ASTM standards

The use of a 6 mm diameter impactor shape instead of the 16 mm impactor standard for an ASTM test setup can raise questions about whether the damage area is sufficiently representative for a reliable comparison of residual strength and stiffness. The ASTM standard used for CAI specifies a 100 by 150 mm specimen damaged by a 16 mm diameter hemispherical impactor. [43] Due to the constraints imposed by the use of airsoft commercial parts, the impactor shape in this study was limited to a 6 mm sphere. For consistency, the DWIT impactor was also adjusted to a 6 mm diameter hemisphere.

In the study by Içten et al. [62], the effect of impactor diameter on the low-velocity impact response and the subsequent compression-after-impact (CAI) behavior was investigated. Their findings showed that the CAI strength generally increases with increasing impactor diameter for the same impact energy. Based on this conclusion, the results of the CAI test in this study might be expected to lower strength and stiffness values compared to results obtained using larger impactors. However, it is worth noting that the smallest impactor used in their study had a diameter of 12.7 mm, which is still significantly larger than the 6 mm diameter used in this research. This discrepancy introduces additional uncertainty when comparing the results of this study to those in the existing literature.

Further research into the effects of smaller impactor diameters on CAI performance is limited, making it difficult to conclusively determine the extent to which deviating from the standard impactor size affects the results. Investigating the influence of impactor size on both the damage mechanisms and the CAI strength would help bridge this knowledge gap. It is recommended that future studies include a systematic evaluation of varying impactor diameters, including sub-12.7 mm sizes, to better understand their effects on CAI test results and improve the reliability of non-standard testing setups.

6.4 Aluminium pellet results

The results of the aluminium pellets are not within the 95% confidence interval of the fitted curve of the E-N data. This suggests that the impactor material plays a significant role in the response, indicating that different materials may lead to varying outcomes. The main differences between the aluminium and the steel pellet results are the impact velocity between the aluminium and steel pellets, as well as differences in material type and impact energy.

In this research, surface microscopy of the layers was conducted, and in Figure 6.3, microscopy images for 0.5N damage fractions of both aluminium (0.88 J) and steel pellets (1.75 J) are shown.

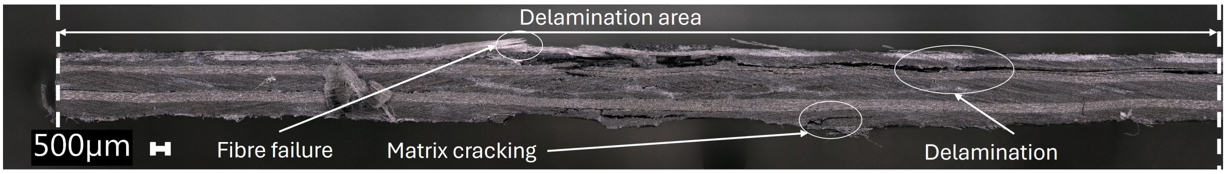

(a) REG 0.88J microcopy surface picture, shot with aluminium pellets

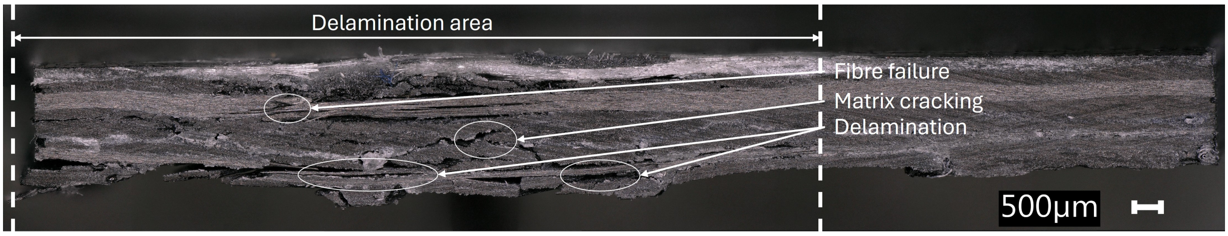

(b) REG 1.75J microscopy surface picture, shot with steel pellets

Figure 6.3: Optical microscopy picture of the inside layers of the REG material for 0.88J and 1.75J and 0.5N damage fraction

In Figure 6.3a, the material shows large delamination between the top layer and the layer below, a hole caused by matrix failure and fibre failure at the impact locations, and significant delamination on the bottom layer. In Figure 6.3b, similar failure mechanisms are observed. However, compared to the 0.88 J case, the matrix cracking and fibre failure appear more pronounced within the layers. Additionally, for the 0.88 J case, the top surface exhibits an eroded hole, which is not present in the 1.75 J case.

The higher strain rate, due to the increased impact velocity, may explain this stiffer material response. As explained in subsubsection 2.6.3, a higher strain rate can reduce the time for the material to respond to the impact, leading to more brittle behavior compared to lower strain rates. [34]

The density and hardness of aluminium are significantly lower than those of steel. Research by Lamontagne et al. [63] found that the impact damage in composites is independent of the projectile density and significantly influenced by velocity. In the study of Goldsmith [64] the influence of projectile hardness was researched. This research concludes that material hardness plays a critical role in determining impact damage characteristics. Hardened projectiles tend to exhibit greater energy loss upon impact compared to softer counterparts, leading to increased fragmentation and larger crater dimensions. The disparity in hardness between the projectile and target significantly affects outcomes, with closely matched hardness levels amplifying deformation and energy absorption. [64] Based on the density and hardness difference, the aluminium pellets should not have penetrated as early as observed in the study. The difference in velocity could explain the lower number of impacts for the aluminium pellets than predicted by the fitted curve. However, this behavior still needs further investigation.

6.5 DWIT relation results

The results of the DWIT relation plots, in Figure 5.5, showed some unexpected behavior. The first one or two impacts had a lower maximum force than the next few impacts. For the absorbed energy it was the inverse of this. It was expected that the absorbed energy would increase, and the maximum force would decrease over the number of impacts. In the study of Jang [65], they found a similar behavior in their DWIT tests.

In their study[65] they explained that a critical incident energy exists. This critical incident energy represents the threshold above which damage begins to occur in a composite material subjected to low-energy impacts. Below this threshold, the composite absorbs the incident energy "elastically", responding by bending without initiating damage mechanisms such as delamination. Damage mechanisms as matrix cracking and indentation could already happen at an energy below this threshold value.[65]

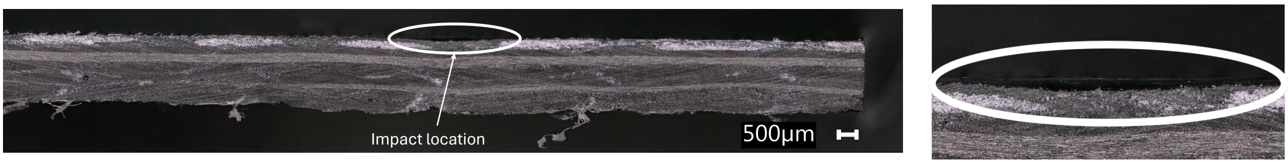

(a) REG material impacted with one 4.0 J impact layers cut off at impact point optical microscopy picture

(b) Zoomed-in picture of the impact point

Figure 6.4: REG material impacted with one 4.0J impact layer microscopy and zoomed-in picture on impact point

In Figure 6.4a the microscopy picture of a cut-off at the impact location for a 4.0J impact is shown. Inspecting Figure 6.4a there is no delamination shown, only a small indentation upon close inspection in Figure 6.4b. The theory of the critical indentation energy aligns with these observations. This finding confirms that the incident energy of the first impact was below the threshold value, allowing the composite to accommodate the impact without structural failure. As further impacts were applied, the accumulated energy to the composite likely exceeded the critical incident energy, initiating damage mechanisms. The increase in maximum force and decrease in absorbed energy observed after the first impact may be the composite's resistance to the initial progression of damage. Once sufficient damage accumulated the structural stiffness began to degrade, leading to a gradual decrease in maximum force and increase in absorbed energy with additional impacts.

7 Conclusion

This research was conducted to get a better understanding of the failure modes and impact fatigue characteristics of commercially used composite sandwich structures subjected to repetitive low-velocity impact loads, with a focus on their application in the hull of high-speed crafts operating in low-ice conditions. Through a combination of drop weight impact tests (DWIT), a single point impact fatigue test (SPIFT), and compression after impact (CAI) tests, the behavior of quasi-isotropic carbon fibre-reinforced epoxy materials with and without a single-sided glass fibre-reinforced layers was evaluated.

The results revealed that top sheet failure of the full sandwich structure was the primary failure mode at the macro scale, with matrix cracking, fibre failure, and delamination observed on the microscale. A difference in shape and size of the delamination area was found depending on the magnitude of the energy impact, with lower energy impacts causing larger areas of delamination around the impact point.

E-N curves constructed from DWIT and SPIFT results provided a clear representation of the regular lay-up, with and without the sacrificial layer, impact fatigue behaviour. The use of a sacrificial layer showed a benefit at high-energy impacts, increasing penetration energy and the number of impacts to failure at similar high energy levels. However, at lower energy levels, the addition of the sacrificial layer did not result in a notable difference, as both material types displayed similar performance.

The CAI tests tried to quantify residual strength and stiffness but showed no clear trend across damage fractions, while a slight decrease in strength was observed between undamaged and fully damaged samples. The 1.75J and 1.17J CAI tests showed a significant decrease in strength. This complements the findings of the larger delamination area in microscopy picture. However, the lack of a clear trend limits ability to draw strong conclusions on the behavior of residual strength and stiffness. Further investigation or alternative testing setups are recommended to better understand residual strength and stiffness trends in these materials.

The first key design guideline is that the experimental results indicate using SAC material is advantageous for withstanding high-impact energy scenarios. For the low impact energy part of the curve, the comparison between the REG and SAC materials revealed no significant difference. Another key design recommendation is that multiple low-energy impacts result in a significantly larger damage region around the impact location compared to high-energy impacts for the same level of damage fraction. This larger damage region includes not only delamination but also fibre and matrix failure. Consequently, the structural strength is substantially lower at the same damage fraction following low-energy impacts than high-energy impacts. Additionally, there is a contradiction to consider: while it might seem beneficial to only experience small impacts, this actually results in the material becoming progressively weaker compared to high-energy impacts. Therefore, an optimum balance must be found to ensure the material maintains its structural integrity over time.

To conclude, this study has shown that repetitive low-velocity impact loads significantly influence the failure modes and impact fatigue characteristics of composite sandwich structures used in high-speed crafts operating in low-ice conditions. The failure mode on macro scale observed was top sheet failure, accompanied by matrix cracking, fibre failure, and delamination at the microscale. The presence of a sacrificial layer was beneficial at high-energy impacts, enhancing penetration energy and the number of impacts to failure, although it had minimal effect at lower energy levels. At lower energy levels the damage area around the impact location drastically increases and consequently the strength of the structures significantly decreases. The CAI tests indicated that residual strength and stiffness did not show significant trends across damage fractions, suggesting the need for further investigation. At last, two key design recommendations were created based on the experimental results and the literature for further improvement of designing composites against low energy impact loads. Overall, these findings contribute to a deeper understanding of the durability and longevity of composite sandwich structures in maritime applications.

8 Recommendations

In this section the recommendations in this research are listed and elaborated on.

8.1 Turned material

The first recommendation is based on the lay-up order of the asymmetrical SAC material. During the testing phase, the lay-up was reversed to determine if the impact characteristics would significantly change due to the asymmetrical lay-up. The results of these drop weight impact tests are shown in Figure 8.1 in comparison to the SAC fit and the 95% confidence interval.

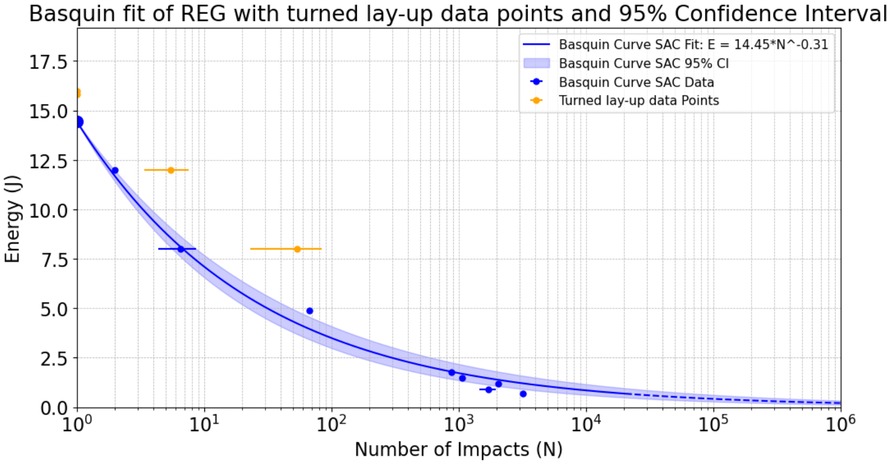

Figure 8.1: Results of the Turned lay-up in comparison to the SAC material

The results indicate that the reversed material lay-up has promising impact fatigue characteristics. Placing the sacrificial layer on the bottom positively affects the energy absorbed by the material. This results in a higher number of impacts until failure at all energy levels and a higher initial number for the E-N curve. Further research into the impact response of low-energy impacts on the reversed lay-up is recommended, as this could be beneficial for hull design.

8.2 Life prediction model on literature models and experimental results

Another recommendation is based on a life prediction model that could be developed using the experimental results of this study and existing literature models discussed in the literature review in subsection 2.5, subsubsection 2.2.2, and subsection 2.3. The literature models of Bridges [14] could be useful for predicting the number of impacts over a certain traveling distance. The model used in the research by Daley [6] can be used to determine the impact energy based on vessel parameters. Combining these models with the experimental data on impact fatigue characteristics provides a solid foundation for developing a life prediction model or tool that could enhance the design process of composite vessels operating in ice conditions. However, developing such a model is not without its challenges. The model used by Daley [6] simplifies the complex six degrees of freedom (6DOF) motion typically experienced by vessels during ice interactions into a single degree of freedom (1DOF) model. This simplification limits its ability to capture the full range of vessel dynamics, making direct comparisons with experimental data challenging. Additionally, the diameter of the impact surface has a significant effect on the extent of damage to the composite sample. As a result, normalizing the impact diameter is essential for ensuring accurate and meaningful comparisons between different test scenarios.

Further research could focus on validating the model with real-world data and exploring additional factors that influence impact fatigue in composite materials.

8.3 Palgrem Miner's rule

It would have been valuable to investigate the applicability of Palmgren Miner's rule [66] for impact fatigue in composite materials. Specifically, exploring whether the linearity of damage accumulation holds under repeated low-velocity impacts would provide insights into the validity of this rule for composites. Given the complex damage mechanisms and non-linear behaviour often observed in composite structures, understanding the extent to which Palmgren Miner's rule can be applied could significantly contribute to predicting their long-term performance under repetitive impact loading conditions.

8.4 Comparability of SPIFT and DWIT Results and Effects of aluminium Pellets

To reinforce the conclusion that the results of the SPIFT and DWIT are comparable, it is recommended to conduct research allowing for overlapping results. Such a study would provide definitive evidence of the comparability between both setups, advancing and standardizing the SPIFT test methodology. Additionally, the use of aluminium pellets introduces complexity to damage mechanisms. Despite aluminium being softer and less dense, the specimens were penetrated prematurely, likely due to increased impact velocity. Further research is recommended to investigate the failure mechanics associated with aluminium impacts to better understand this behavior and its implications for testing standards.

8.5 Factors Affecting CAI Test Accuracy and Impact of Impactor Size on CAI Strength

The results of the CAI test may have been affected by the small thickness of the specimens, out-of-plane deformations, and buckling failure modes. These factors likely compromised the accuracy of the CAI test outcomes. To address these issues, the use of an alternative test apparatus or one of the test methods discussed in subsection 6.2 is strongly recommended. Additionally, investigating the influence of impactor size on damage mechanisms and CAI strength is essential to bridging the existing knowledge gap. Future studies should include a systematic evaluation of different impactor diameters, particularly sizes smaller than 12.7 mm. Such research would help clarify how varying impactor dimensions affect CAI test results and further refine testing protocols.

References

[1] W. M. Organization, "Sea-ice information and services," 2021.

[2] F.-S. I. C. RULES, "The structural design and engine output required of ships for navigation in ice," 2021.

[3] G. W. Timco and W. F. Weeks, "A review of the engineering properties of sea ice," *Cold Regions Science and Technology*, vol. 60, pp. 107–129, 2 2010.

[4] N. O. Niclasen, "Light weight marine vessels operating in brash ice," 2015.

[5] C. Daley, "Energy based ice collision forces," 1999.

[6] C. G. Daley and C. G. Daley, "Oblique ice collision loads on ships based on energy methods," pp. 67–72, 2001. [Online]. Available: https://www.researchgate.net/publication/287831071

[7] Y. N. Popov, "Strength of ships sailing in ice," 1969.

[8] S. Idrissova, M. Bergström, S. E. Hirdaris, and P. Kujala, "Analysis of a collision-energy-based method for the prediction of ice loading on ships," *Applied Sciences (Switzerland)*, vol. 9, 11 2019.

[9] DNV, "Rules for classification," 2020.

[10] BV, "Rules for the classification of ships," 2022.

[11] D. M. Masterson and R. M. W. Frederking, "Local contact pressures in ship/ice and structure/ice interactions," pp. 169–185, 1993.

[12] R. S. Taylor, I. J. Jordaan, C. Li, and D. Sudom, "Local design pressures for structures in ice: Analysis of full-scale data," *Journal of Offshore Mechanics and Arctic Engineering*, vol. 132, pp. 1–7, 8 2010.

[13] M. S. Rahman, R. S. Taylor, A. Kennedy, A. S. Ré, and B. Veitch, "Probabilistic analysis of local ice loads on a lifeboat measured in full-scale field trials," *Journal of Offshore Mechanics and Arctic Engineering*, vol. 137, 2015.

[14] I. S. of Offshore and P. Engineers., *The proceedings of the twenty-first (2011) International Offshore and Polar Engineering Conference : Maui, Hawaii, USA, June 19-24, 2011*. International Society of Offshore and Polar Engineers, 2011.

[15] W. J. Stronge, *Collision against Flexible Structures*. Cambridge University Press, 2 2010, pp. 201–218.

[16] ——, *Introduction to Analysis of Low Speed Impact*. Cambridge University Press, 2 2010, pp. 1–20.

[17] R. Bridges, K. Riska, and S. Zhang, "Fatigue assessment for ship hull structures navigating in ice regions," *Proceedings of the Icetech*, pp. 355–360, 2006.

[18] P. Varsta, "On the mechanics of ice load on ships in level ice in baltic sea," 1983.

[19] K. Riska and J. Kämäräinen, "A review of ice loading and the evolution of the finnish-swedish ice class rules," 2011. [Online]. Available: https://www.researchgate.net/publication/289394868

[20] A. Suyuthi, B. J. Leira, and K. Riska, "Fatigue damage of ship hulls due to local ice-induced stresses," *Applied Ocean Research*, vol. 42, pp. 87–104, 8 2013.

[21] "Review of composite materials and applications," *Materials Today: Proceedings*, 10 2023.

[22] R. Hsissou, R. Seghiri, Z. Benzekri, M. Hilali, M. Rafik, and A. Elharfi, "Polymer composite materials: A comprehensive review," 4 2021.

[23] R. Nijssen, *Composite Materials an introduction*, 3rd ed., 2015.

[24] I. S. Abbood, S. A. Odaa, K. F. Hasan, and M. A. Jasim, "Properties evaluation of fiber reinforced polymers and their constituent materials used in structures - a review," vol. 43. Elsevier Ltd, 2021, pp. 1003–1008.

[25] J. G.-J. R. P. John Summerscales, *Marine Composites: Design and Performance*. Woodhead Publishing, 2018.

[26] B. V. Ramnath, K. Alagarraja, and C. Elanchezhian, "Sciencedirect review on sandwich composite and their applications," 2019. [Online]. Available: www.sciencedirect.comwww.materialstoday.com/proceedings

[27] T. C. Triantafillou and L. J. Gibson, "Failure mode maps for foam core sandwich beams," pp. 37–53, 1987.

[28] I. M. Daniel and E. E. Gdoutos, *Failure Modes of Composite Sandwich Beams*. Springer Netherlands, 2009, pp. 197–227.

[29] W. G. Heath, "Sandwich construction, part 2: The optimum design of flat sandwich panels," *Aircraft Engineering*, vol. 32, pp. 230–235, 1969.

[30] E. E. Gdoutos, I. M. Daniel, and R. R. Mccormick, "Failure mechanisms of composite sandwich structures," 2009. [Online]. Available: https://www.researchgate.net/publication/252673934

[31] A. Shipsha, S. H. Hallstro¨, Hallstro¨m, , and D. Zenkert, "Failure mechanisms and modelling of impact damage in sandwich beams-a 2d approach: Part i-experimental investigation," 2003.

[32] G. Bragagnolo, A. D. Crocombe, S. L. Ogin, I. Mohagheghian, A. Sordon, G. Meeks, and C. Santoni, "Investigation of skin-core debonding in sandwich structures with foam cores," *Materials and Design*, vol. 186, 1 2020.

[33] T. S. Lim, C. S. Lee, and D. G. Lee, "Failure modes of foam core sandwich beams under static and impact loads," *Journal of Composite Materials*, vol. 38, pp. 1639–1662, 2004.

[34] M. Sadighi and R. Alderliesten, "Impact fatigue, multiple and repeated low-velocity impacts on frp composites: A review," 10 2022.

[35] D. Banhart, S. Monir, O. Durieux, R. J. Day, M. Jones, N. Luhyna, and Y. Vagapov, "A review of experimental and numerical methodologies for impact testing of composite materials," *Sensing Technology*, vol. 2, 12 2024.

[36] Y. Pai, K. D. Pai, and M. V. Kini, "A review on low velocity impact study of hybrid polymer composites," *Materials Today: Proceedings*, vol. 46, pp. 9073–9078, 1 2021.

[37] A. Mustafa, M. A. Mahmoud, A. Abdulraheem, S. A. Furquan, A. Al-Nakhli, and M. BaTaweel, "Comparative analysis of static and dynamic mechanical behavior for dry and saturated cement mortar," *Materials*, vol. 12, 10 2019.

[38] M. You, M. B. Li, Y. L. Yuan, G. Lin, F. W. Ma, L. F. Du, and S. J. Tang, "Review of experimental techniques for impact property of adhesive bonds," *International Journal of Adhesion and Adhesives*, vol. 100, 7 2020.

[39] R. Bardenheier and G. Rogers, "Dynamic impact testing with servohydraulic testing machines," vol. 134, 8 2006, pp. 693–699.

[40] K. A. Kamarudin and I. A. Hamid, "Effect of high velocity ballistic impact on pretensioned carbon fibre reinforced plastic (cfrp) plates," vol. 166. Institute of Physics Publishing, 1 2017.

[41] H. K. Kim, B. S. Kang, and J. Kim, "Muzzle velocity estimation of an electromagnetic launcher using b-dot probe," *International Journal of Applied Electromagnetics and Mechanics*, vol. 61, pp. 563–580, 2019.

[42] N. Johansen, "Test methods for evaluating rain erosion performance of wind turbine blade leading edge protection systems," 2020.

[43] "Designation: D 7137/d 7137m-07 standard test method for compressive residual strength properties of damaged polymer matrix composite plates 1." [Online]. Available: www.astm.org,

[44] M. Richardson and M. Wisheart, "Review of low-velocity impact properties of composite materials," *Composites Part A: Applied Science and Manufacturing*, vol. 27, pp. 1123–1131, 1996.

[45] G. Davies and P. Irving, *Impact, post-impact strength and post-impact fatigue behaviour of polymer composites*. Elsevier Inc., 2015, pp. 231–259.

[46] D. Broek, *Elementary Engineering Fracture Mechanics*. Sijthoff Noordhoff, 1978.

[47] M. Kawai and A. Hachinohe, "Two-stress level fatigue of unidirectional fiber-metal hybrid composite: Glare 2," pp. 567–580, 2002. [Online]. Available: www.elsevier.com/locate/ijfatigue

[48] I. Burhan and H. S. Kim, "S-n curve models for composite materials characterisation: An evaluative review," 9 2018.

[49] A. Trudel, M. Turgeon, E. Aecom, C. East, and I. Lanctôt, "Recent trends in the design of hydropower components subjected to cycling and fatigue; towards improved technical design specifications," 2017. [Online]. Available: https://www.researchgate.net/publication/320310804

[50] O. Basquin, "The exponential law of endurance test." *ASTM STP*, vol. 10, p. 625630, 1910.

[51] P. Shabani and N. Shabani, "Fatigue life prediction of high-speed composite craft under slamming loads using progressive fatigue damage modeling technique," *Engineering Failure Analysis*, vol. 131, p. 105818, 1 2022.

[52] E. N. Eliopoulos and T. P. Philippidis, "A progressive damage simulation algorithm for gfrp composites under cyclic loading. part ii: Fe implementation and model validation," *Composites Science and Technology*, vol. 71, pp. 750–757, 3 2011.

[53] M. M. Shokrieh and L. B. Lessard, "Multiaxial fatigue behaviour of unidirectional plies based on uniaxial fatigue experiments m i. modelling," pp. 201–207, 1997.

[54] "Standard test method for measuring the damage resistance of a fiber-reinforced polymer matrix composite to a drop-weight impact event 1." [Online]. Available: www.astm.org,

[55] J. SELWYN D. SMITH, *INTERDR BALLISTICS OF GUNS*. UNITED STATES ARMY MATERIET COMMAND, 1965, ch. 2, pp. 3–54.

[56] R. K. Mobley, *FORCES IN LIQUIDS*. Elsevier, 2000, pp. 8–24.

[57] A. T. Nettles and S. M. Hromisin, “Normalization of impact energy by laminate thickness for compression after impact testing,” 2013. [Online]. Available: http://www.sti.nasa.gov

[58] C. W. Bert, *Classical Lamination Theory*. Springer Netherlands, 1989, pp. 11–16.

[59] H. B. S. P, “Compression after impact: the 5,000 data point!” *Proceedings of the 34th international SAMPE symposium*, pp. 1411–1421, 5 1989.

[60] S. Sanchez-Saez, E. Barbero, R. Zaera, and C. Navarro, “Compression after impact of thin composite laminates,” *Composites Science and Technology*, vol. 65, pp. 1911–1919, 10 2005.

[61] Airbus, “Aitm1-0075 airbus test method. fibre reinforced plastics. constant amplitude fatigue test on coupons,” 2012.

[62] B. M. Icten, B. G. Kiral, and M. E. Deniz, “Impactor diameter effect on low velocity impact response of woven glass epoxy composite plates,” *Composites Part B: Engineering*, vol. 50, pp. 325–332, 7 2013.

[63] C. G. Lamontagne’, G. N. Manuelpillai’, J. H. Kerr, E. A. Taylor’", R. C. Tennyson’, and M. J. Burchell’, “Projectile density, impact angle and energy effects on hypervelocity impact damage to carbon fibre/peek composites,” pp. 381–398, 2001. [Online]. Available: www.elsevier.com/locate/ijimpeng

[64] W. Goldsmith, “Non-ideal projectile impact on targets,” pp. 95–395, 1999.

[65] B. Jang, W. Kowbel, and B. Jang, “Impact behavior and impact-fatigue testing of polymer composites,” *Composites Science and Technology*, vol. 44, pp. 107–118, 1 1992.

[66] A. Palmgren, “Die lebensdauer von kugellagern,” *Zeitschrift des Vereines Deutscher Ingenieure*, vol. 68, 1924.

A Appendix

Due to its size, the dataset created during this research could not be included in the appendix of this master's thesis. Instead, it has been securely stored on an external drive. For access, please contact dr.ir. T.H. Hoksbergen.

Similarity Report ID: oid:6294:264506276

PAPER NAME	AUTHOR
Master_Thesis_AukeJaspars.pdf	Auke Jaspers

WORD COUNT	CHARACTER COUNT
22587 Words	115634 Characters
PAGE COUNT	**FILE SIZE**
68 Pages	20.7MB
SUBMISSION DATE	**REPORT DATE**
Feb 11, 2025 10:30 AM GMT+1	Feb 11, 2025 10:31 AM GMT+1

● 11% Overall Similarity

The combined total of all matches, including overlapping sources, for each database.

- 8% Internet database
- Crossref database
- 0% Submitted Works database
- 7% Publications database
- Crossref Posted Content database

● Excluded from Similarity Report

- Bibliographic material
- Small Matches (Less then 8 words)
- Cited material